14 Stretch Shaping

14.1 Fiber Spinning, 824
14.2 Film Blowing, 836
14.3 Blow Molding, 841

In this chapter we discuss three common and important stretch or extensional flow-based shaping operations: *melt fiber spinning*, *tubular film blowing*, and *blow molding*. These operations take place downstream from the die. Another stretch-flow–type shaping method is thermoforming, which involves deformation of previously shaped polymer sheets or films into a desired shape. Since the principles of thermoforming are very similar to those of parison inflation discussed later in this chapter, we do not dwell on this shaping method.

Fiber spinning is a uniaxial extensional deformation process, which is the principal method of manufacturing synthetic fibers for the textile industry. It also provides a good example of the enormous significance of "structuring" polymeric chains during shaping for imparting unique properties to a product. In fact, fiber spinning is the quintessential example of the goal of modern polymer processing as a multidisciplinary activity, better termed "macromolecular engineering," whose objective, as discussed in Chapter 1, is: "to bridge the gap between science and technology in material processing using modeling and computation of the full thermomechanical history during formation to quantitatively predict properties" (1).

Film blowing and blow molding are shaping operations that produce most plastics films, bags, and bottles, respectively. Both processes involve two-dimensional elongational deformation of the polymer melt. Thermoforming is a versatile, relatively inexpensive shaping method used extensively for packaging applications, which also involves two-dimensional extensional deformation. In all these processes, the purpose of a mathematical analysis is to describe the kinematics and dynamics of the process, to predict the nature and source of instabilities that are characteristic of these unconfined deformation processes, and, as just stated, hopefully predict a priori final properties based on the thermal and deformational history.

14.1 FIBER SPINNING

Until the 20th century mankind was limited to natural fibers such as wool, cotton, linen, and for the rich, silk. The first man-made fiber was artificial silk rayon (1910), which was based on cellulose. The big jump came with the invention of nylon by Wallace Carothers, with commercial production starting in 1939, followed in the 1950s by acrylics (which, when mixed with cotton, produced the "wash-and wear" textiles), polyesters, and many others.

Principles of Polymer Processing, Second Edition, by Zehev Tadmor and Costas G. Gogos.
Copyright © 2006 John Wiley & Sons, Inc.

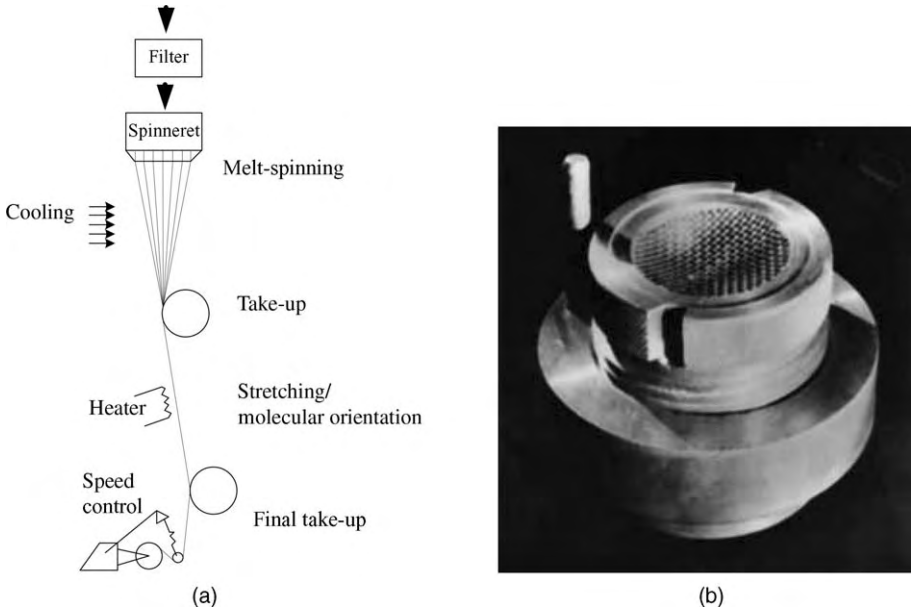

Fig. 14.1 (a) Schematic representation of the melt fiber spinning process. (b) Photograph of a spinneret. [Fiber-world Classroom Website.]

The melt spinning of fibers begins with the melting and pumping of solid pellets by a screw extruder (normally followed by a gear pump for accurate flow-rate control) into a die with multiple holes called a *spinneret*. The extruded strands are drawn and the solidified fibers are wound up and subsequently cold-drawn further, as shown schematically in Fig. 14.1(a). The design of a commercial spinneret is shown in Fig.14.1(b). In addition to melt spinning, there are two other spinning methods: *wet spinning*, in which the polymer is dissolved in a solvent and extruded through a spinneret immersed in a chemical solution, and *dry spinning*, which also extrudes a solution of the polymer the solvent of which evaporates upon exiting the spinneret. These are used for polymers that cannot be melt-spun. However, in this chapter we discuss only the ubiquitous and most commercially important melt spinning.

In analyzing the melt spinning process, we consider a single strand as it emerges from the spinneret and is drawn by the take-up roll, as shown in Fig. 14.2. There is no clear point of demarcation where post–die extrudate swelling ends and melt stretching begins. The two phenomena occur simultaneously, especially near the die exit, where the rapid rate of swelling ordinarily occurs. Experimental data from actual melt-spinning runs indicate that the melt strand cross-sectional area decreases hyperbolically from the spinneret exit to the take-up rolls (2). Figure 14.3 gives typical melt strand area and radius axial profiles. The melt drawdown region extends to about 200 cm from the spinneret exit. There is no specific indication of where the melt strand begins to solidify (''frost line'').

The final properties of the fiber, such as tenacity,[1] modulus, luster, and flex loss, are determined by the spinning process. This is because, as the molten filament moves from

1. Tenacity equals the breaking strength (grams) divided by denier. Denier is the weight in grams of 9000 meters of filament.

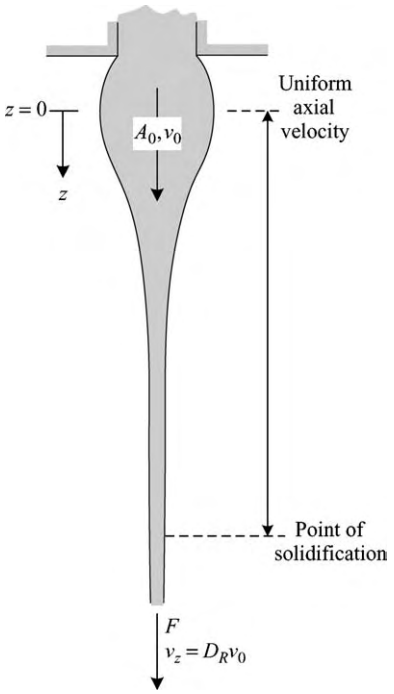

Fig. 14.2 A single strand emerging from the spinneret which undergoes die swell, then cooling to a point of solidification, drawn by the take-up roll.

the spinneret exit to the take-up roll, it is simultaneously stretched and cooled, thus orienting the polymer chains (Fig. 14.4) and crystallizing the polymer; this is repeated with the subsequent drawing and orientation in the solid sate. Therefore, the spinning process is, in fact, not only a fiber forming step, but a ''structuring'' one as well. Early

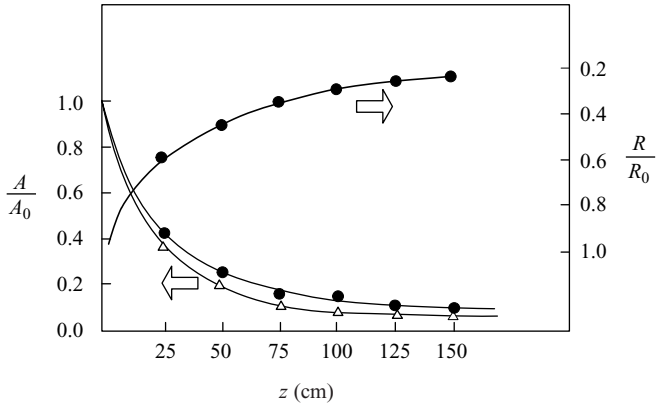

Fig. 14.3 Melt strand area and radius profiles in the melt drawdown region: • nylon 6 at 265°C and take-up velocity of 300 m/min; Δ, polypropylene (PP) at 262°C and take-up velocity of 350 m/min. [Reprinted with permission from H. F. Mark, in *Rheology,* Vol. 4, F. R. Eirich, Ed., Academic Press. New York, 1969.]

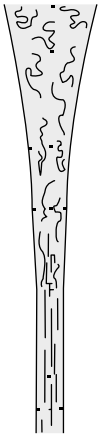

Fig. 14.4 Schematic view of orientation development along the spinline.

work on structuring during fiber spinning was done by Dees and Spruiell (3), who studied structure development with linear high density polyethylene fiber spinning and modeled it as shown in Fig. 14.5. They reported that the observed orientation function behavior during melt spinning can be explained with a morphological model, assuming that at low

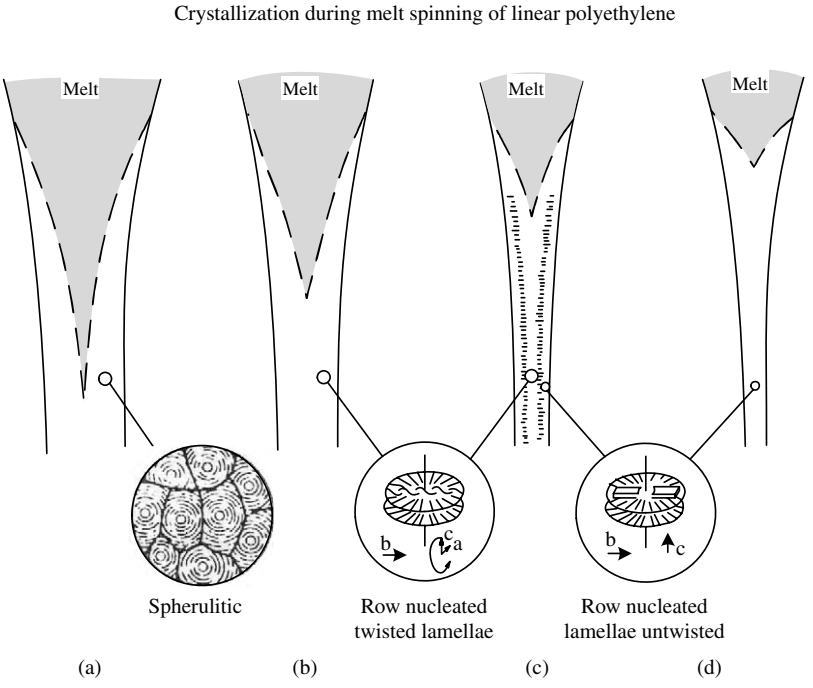

Fig. 14.5 Morphological model of structures developed in as-spun HDPE. Take-up velocities are (a) very low; (b) low; (c) medium; and (d) high. [Reprinted by permission from J. E. Spruiell and J. L. White, "Structure Development during Polymer Processing: Studies of the Melt Spinning of Polyethylene and Polypropylene Fibers," *Polym. Eng. Sci.*, **15**, 660 (1975).]

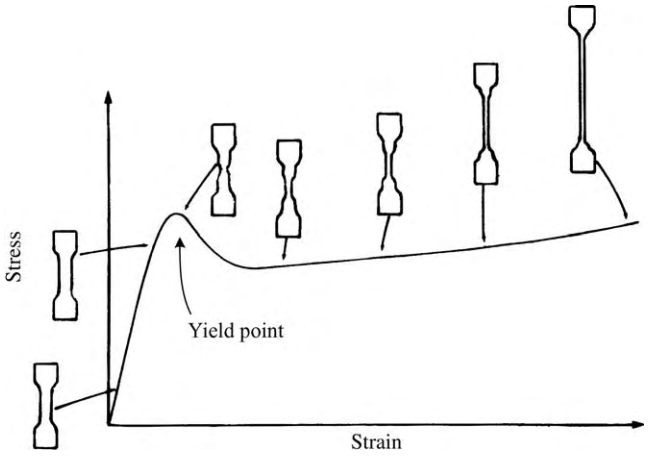

Fig. 14.6 Schematic stress–strain curves for a semicrystalline polymer. The shape of tensile specimens at several stages is indicated. [Reprinted by permission from J. M. Schultz, *Polymer Materials Science*, Prentice Hall, Englewood Cliffs, NJ, 1974.]

spinline stresses or take-up velocities, spherulitic structures are obtained. Increasing the take-up velocity results in row nucleated twisted lamellae, and at even higher speeds, in row nucleated untwisted lamellae.

As noted in Fig.14.1(a), commercial fibers of semicrystalline polymers are always cold-drawn after spinning to achieve further structuring through further macromolecular orientation and crystalline morphological changes, many of which are retained because of the low temperature of the cold-drawing processes. A typical stress–strain curve for a polycrystalline polymer at a temperature $T_g < T < T_m$ appears in Fig. 14.6.

The onset of yielding and necking of fibers, as well as films and tensile bar specimens, is the result of the ability of polycrystalline ''composites'' to accommodate stress-induced destruction of the crystalline units. In this process both the amorphous and the crystalline phases are involved. A ''molecular'' descriptive model of the morphological changes initiated with necking, and propagated by cold drawing, indicated in Fig. 14.7, consists of the following steps:

1. The lamellae slip rigidly past one another. Lamellae parallel to the direction of draw cannot slip; thus, spherulites become anisotropic. At this stage, at which necking begins, the strain is accommodated almost entirely by the interlamellar amorphous component.
2. Since the amorphous ''ties'' are almost completely extended, slip-tilting of the lamellae is induced.
3. Lamellar breakup occurs through chain pulling and unfolding; the chains pulled still connect the fragments of the lamellae.
4. The lamellar fragments slip further in the direction of draw and become aligned. They now form fibrils of alternating crystal blocks and stretched amorphous regions, which may also contain free chain ends, and some chain folds. Thus, the lamellae break into fragments that end up stacked in the axial direction. Tie molecules that connect these fragments in the draw direction provide the strength of the microfibrils in the fiber. Thus the goal in a fiber structuring operation is to employ the values of the parameters of spinning and drawing processes, which increase the fraction of tie molecules.

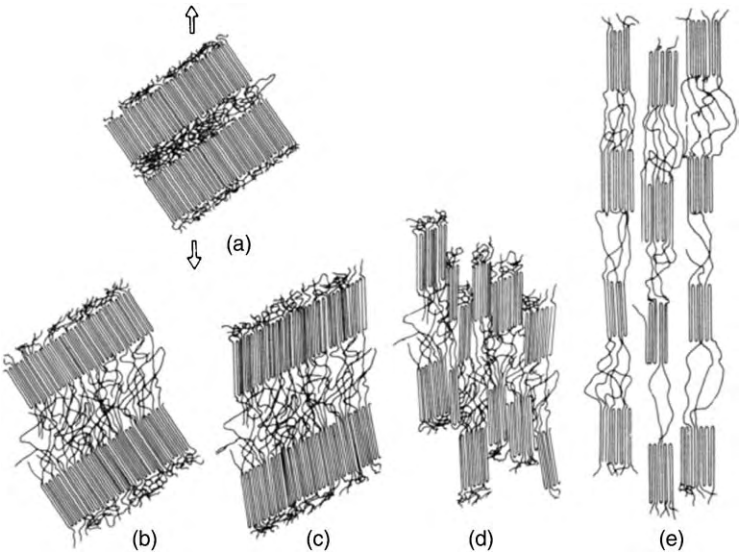

Fig. 14.7 Steps in the deformation of semicrystalline fiber, shown schematically. [Reprinted by permission from J. M. Schultz, *Polymer Materials Science*, Prentice Hall, Englewood Cliffs, NJ, 1974.]

It is evident from the preceding that the important cold drawing variables are not only the rate of extension, determining $t_{\text{exp}} = 1/\dot{\varepsilon}$, and the temperature; determining the relaxation time, λ, but also the initial crystalline morphology, that is, the morphology obtained during the spinning process (see Fig. 14.5). Capaccio and Ward (4) demonstrated the important role played by the initial crystalline morphology in obtaining ultrahighly drawn and ultrahigh stiffness high density polyethylene (HDPE) fibers and films. A HDPE of $\overline{M}_n = 13{,}350$ and $\overline{M}_w = 67{,}800$, cooled from 160°C and quenched at 110°C, possessed an initial morphology such that, when drawn at 75°C at 10 cm/min, it can be extended to a draw ratio of 30. The cold-drawn sample had a specific Young's modulus in tension $E = 68 \times 10^9\ \text{N/m}^2$, an order of magnitude higher than of conventionally drawn HDPE. For comparison, "E" glass fibers have a specific Young's modulus of 35 (N/m^2) and Kevlar fibers, 92 (N/m^2). It should be noted, however, that the theoretical estimates of Young's modulus for fully extended HDPE chains range from 240 N/m^2 to 350 N/m^2 (4). Thus, further structuring improvements are possible, in principle.

The mathematical formulation of the fiber-spinning process is meant to simulate and predict the hydrodynamics of the process and the relationship between spinning conditions and fiber structure. It involves rapid extensional deformation, heat transfer to the surrounding quenching environment, air drag on the filament surface, crystallization under rapid axial-orientation, and nonisothermal conditions.

Example 14.1 A Semiempirical, Simplified, One-Dimensional, Nonisothermal Model [C. D. Han, *Rheology in Polymer Processing*, Academic Press, New York, 1976, Section 12.3.1.] Assuming steady state and further assuming that there is only one nonvanishing velocity component $v(z)$, which is a function of only z, and that temperature varies only in the z direction, the equation of motion reduces to

$$v_z \frac{dv_z}{dz} = -v_z \frac{d}{dz}\left(\frac{\tau_{zz}}{\rho v_z}\right) - 2\left(\frac{\pi v_z}{\rho G}\right) F_D + g_z \qquad \text{(E14.1-1)}$$

where $G = \rho\pi R^2 v_z$ is the mass flow rate and F_D is the air drag force per unit area given by:

$$F_D = \left(\frac{0.843}{\pi R^2}\right)\left(\frac{\rho_a}{\rho}\right) G v_z \left[\frac{\pi\rho\mu_a}{\rho_a}\frac{(L-z)}{G}\right]^{0.915} \tag{E14.1-2}$$

indicating that extension rate is controlled by tensile stresses, air drag on the fiber, and gravitational forces. Similarly, the equation of energy reduces to

$$\frac{dT}{dz} = -\frac{2}{C_v}\left(\frac{\pi}{\rho G v_z}\right)^{1/2}[h(T - T_a) + \sigma\varepsilon(T^4 - T_a^4)] \tag{E14.1-3}$$

In this equation, h is the heat transfer coefficient given by

$$\frac{hR}{k_a} = 0.21(1 + K)\left(\frac{2R\rho_a v_z}{\mu_a}\right)^{0.334} \tag{E14.1-4}$$

where K is an adjustable parameter and the subscript a refers to ambient air. According to Eq. E14.1-3 the temperature drop of the fiber depends on heat transfer to the ambient air and radiation losses. Han coupled these transport equations with an empirical ''Power Law in tension'' constitutive equation containing a temperature-dependent viscosity

$$\tau_{zz} = -3\alpha e^{\beta/T}\left[k_1 + k_2\left(\frac{dv_z}{dz}\right)^{n-1}\right]\frac{dv_z}{dz} \tag{E14.1-5}$$

where

$$\alpha = \eta_0 e^{\Delta E/RT_0} = \eta_0 e^{-\beta/T_0} \tag{E14.1-6}$$

This system of equations is solved numerically. The results obtained are physically reasonable up to the axial position where crystallization commences, where the rate of cooling slows down because of the exothermic solidification phenomenon and the rheological properties change sharply.

Many of the early models were one-dimensional, in which the field equations were averaged over the filament cross section. Kase and Matsuo (5,6) were the first to consider nonisothermal (in the stretching direction) fiber stretching. Matovich and Pearson (7) studied Newtonian, shear thinning and second order fluids. Denn at al. (8,9) modeled the process with upper-convected Maxwell constitutive equation. Papanastasiou et al. (10) studied isothermal viscoelastic spinning. Bell and Edie (11), using a finite element method (FEM), computed the two-dimensional temperature profile, assuming a one-dimensional velocity profile and measures of orientation, to obtain the internal stress distribution (12). The single component models were extended by Kulkarni and Beris (13) and Doufas et al. (14) to two component models, accounting for stress-induced crystallization.

A detailed two-dimensional numerical analysis of nonisothermal spinning of viscoelastic liquid with phase transition was carried out recently by Joo et al. (15). They used a mixed FEM developed for viscoelastic flows (16) with a nonisothermal version of the Giesekus constitutive equation (17), the Nakamura et al. (18) crystallization kinetics

model, and the dependence of the crystallization rate on temperature and molecular orientation according to Ziabicki (19). They simulated amorphous polystyrene and fast-crystallizing nylon-6.6. The results indicate that although the kinematics in the thread line are approximately one-dimensional, as assumed by most researchers, the significant radial temperature nonuniformity leads to radially nonuniform viscoelastic stresses, which result in radially nonuniform molecular orientation and strong radial variation of crystallinity.

The polystyrene simulation followed the experiments of Bell and Edie (12) with good agreement. Figure 14.8 shows the simulation results for fiber spinning nylon-6.6 with a draw ratio of 40. The figure demonstrates the wealth of information provided by the model. It shows the velocity, temperature, axial normal stress, and crystallinity fields along the threadline. We see the characteristic exponential-like drop in diameter with locally (radially) constant but accelerating velocity. However, results map out the temperature, stress, and crystallinity fields, which show marked variation radially and axially.

Recent advances in molecular dynamics simulations enabled Levine et al. (20) to take modeling one step further, to the molecular level. They succeeded in simulating from first principles the structure formation of 100 carbon atom polyethylene during uniaxial extension, under a variety of conditions. Figure 14.9 shows the dynamics of extensional deformation below the melting point, beautifully indicating the dynamic development of orientation and order.

Figure 14.10 shows the simulation results of nonisothermal crystallization, during simultaneous deformation and cooling through the melting point, as is the case in fiber spinning, indicating the formation of homogeneous, deformation-induced crystallization nuclei.

The foregoing analyses show, as pointed out earlier, that fiber spinning is perhaps the first process approaching the goal of modern polymer processing as macromolecular engineering. That is, developing a multiscale approach to simulate manufacturing processes using the governing continuum-level equations and operating conditions. Material-specific parameters for those equations are generated from molecular dynamics simulations, to ensure consistent, predictive ability. Crystal growth rates are generated using parameters derived entirely from first principles molecular modeling, over a large range of temperatures and molecular weight. This is shown schematically in Fig. 14.11.

So far, we assumed that the spinning process is stable. In practice, however, spinning instabilities may constrain spinning rates and even curb the possibility of spinning a fiber. Indeed, not all polymers can be melt-spun. Some polymers are easier to spin than others. The *spinnability* of a polymer is related to the stability of the process (21,22), particularly the ability of polymer melts to be drawn without breaking, due to either capillary failure resulting from surface tension–induced breakup into droplets, ''necking'' and ductile failure (23) characteristic to extension-thinning polymers, and/or cohesive fracture (24,25) exhibited by extension-thickening polymers.

A typical instability is *draw resonance*. Physically, the occurrence of draw resonance can be viewed as follows. In the region between the spinneret exit and the take-up rolls there can be a time variation of the total extrudate mass: although the rate of mass entering this region is constant, the rate it leaves is not controlled, since only the take-up speed is regulated, not the fiber diameter. Thus, if the strand thins out near the take-up rolls, the diameter of the strand above it will increase, creating (from the spinneret exit) a thick–thin strand. But the thick portion soon reaches the take-up rolls. Mass leaves the region at a high rate and the strands thin out upstream, creating a thin–thick strand. The process can repeat itself. This may explain the experimental reports that if solidification occurs before

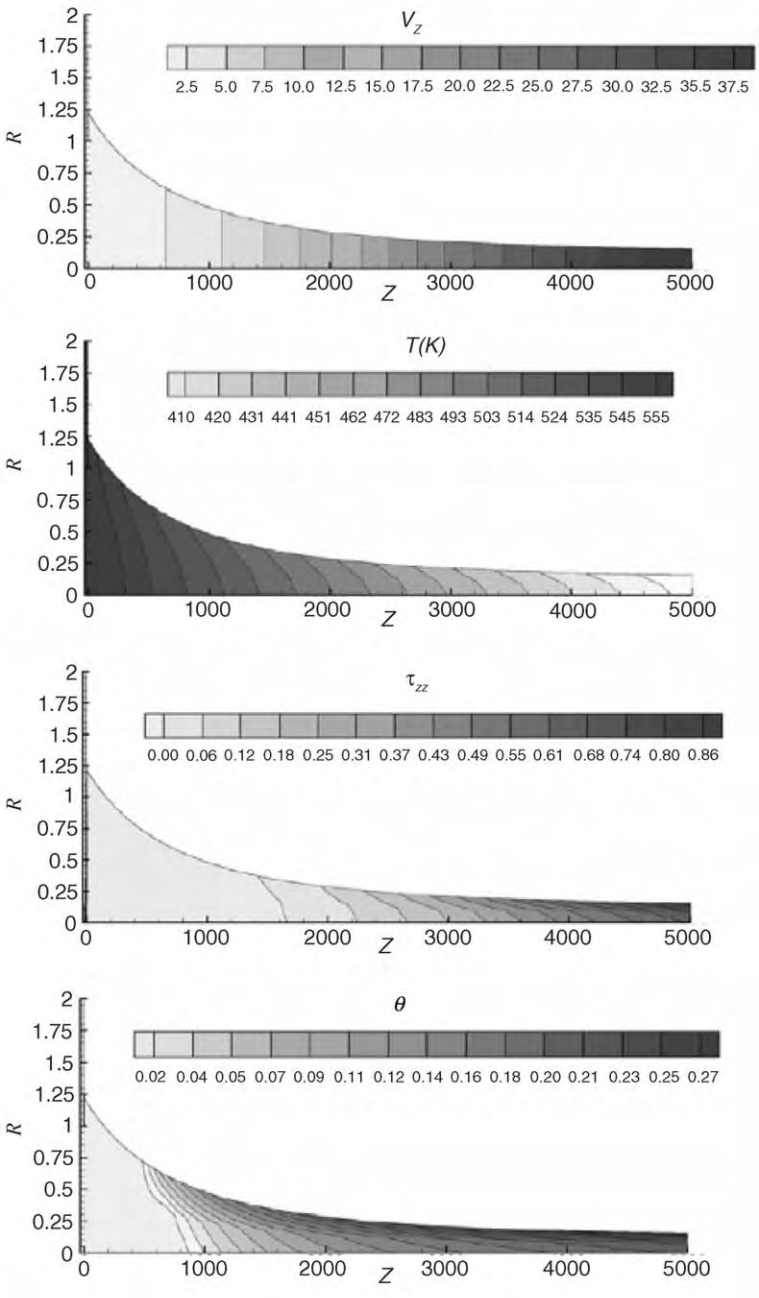

Fig. 14.8 Simulation results for velocity, temperature, axial normal stress, and crystallinity fields for low-speed spinning of nylon-6.6. [Reprinted with permission from Joo et al., "Two-dimensional Numerical Analysis of Nonisothermal Melt Spinning with and without Phase Transition," *J. Non-Newt. Fluid Mech.*, **102**, 37–70 (2002).]

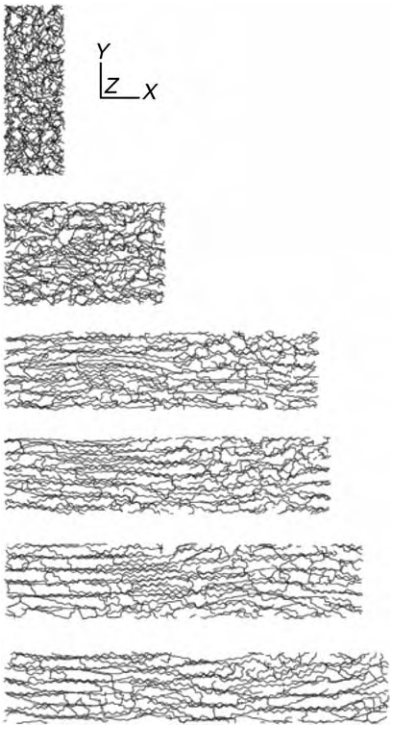

Fig. 14.9 Snapshots of a system of twenty 100 carbon atom long polyethylene chains deformed at 300 K. The initial slab at the top rapidly deforms with the applied stress in the x dimension of the slab, roughly doubling in the first 500 ps to $\lambda = 2.64$ (second image from the top); then the rate of deformation is slower and doubles again in 1500 ps to $\lambda = 5.15$ (third image from the top). Beyond this point the cell deforms even more slowly to reach a final deformation of $\lambda = 6.28$ (bottom image). In absolute values, the initial cell of dimensions $1.88 \times 5.32 \times 5.32$ nm deforms to $11.8 \times 2.23 \times 1.96$ nm. [Reprinted by permission from M. C. Levine, N. Waheed, and G. C. Rutledge, "Molecular Dynamics Simulation of Orientation and Crystallization of Polyethylene during Uniaxial Extension," *Polymer*, **44**, 1771–1779, (2003).]

the take-up rolls, no resonance is observed (26), as well as the observation of increased resonance period with increased residence time in the spinline (21).

Isothermal draw resonance is found to be independent of the flow rate. It occurs at a critical value of draw ratio (i.e., the ratio of the strand speed at the take-up rolls to that at the spinneret exit). For fluids that are almost Newtonian, such as polyethylene terephthalate (PET) and polysiloxane, the critical draw ratio is about 20. For polymer melts such as HDPE, polyethylene low density (LDPE), polystyrene (PS), and PP, which are all both shear thinning and viscoelastic, the critical draw ratio value can be as low as 3 (27). The maximum-to-minimum diameter ratio decreases with decreasing draw ratio and decreasing draw-down length.

The experimental and theoretical literature on instabilities in fiber spinning has been reviewed in detail by Jung and Hyun (28). The theoretical analysis began with the work of Pearson et al. (29–32), who examined the behavior of inelastic fluids under a variety of conditions using linear stability analysis for the governing equations. For Newtonian fluids, they found a critical draw ratio of 20.2. Shear thinning and shear thickening fluids

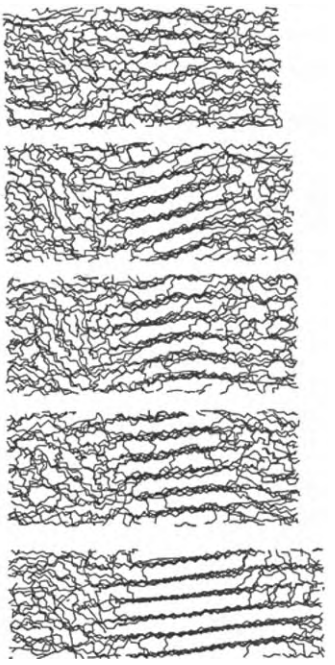

Fig. 14.10 Chain configurations from a nonisothermal deformation simulation. From top to bottom, the images were taken at 374, 368, 364, 360 K, and 290 K, corresponding to 7.6, 8.2, 8.6, 9.0, and 16.0 ns. [Reprinted by permission from M. C. Levine, N. Waheed, and G. C. Rutledge, ''Molecular Dynamics Simulation of Orientation and Crystallization of Polyethylene during Uniaxial Extension,'' *Polymer*, **44**, 1771–1779, (2003).]

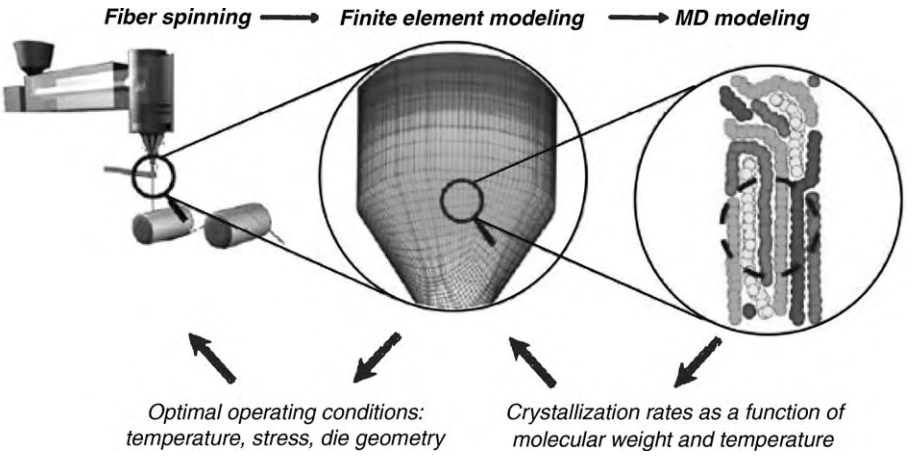

Fig. 14.11 Schematic representation of fiber spinning process simulation scheme showing the multiple scale simulation analysis down to the molecular level. This is the goal of the Clemson University–MIT NSF Engineering Research Center for Advanced Engineering Fibers and Films (CAEFF) collaboration. CAEFF researchers are addressing fiber and film forming and structuring by creating a multiscale model that can be used to predict optimal combinations of materials and manufacturing conditions, for these and other processes.

exhibit critical draw ratios that are smaller or larger, respectively, than 20.2. At the same time, Denn et al. (8,33–36) systematically carried out both infinitesimal (linearized) and finite amplitude analyses of the isothermal draw resonance problem. They found that Newtonian fluids are stable to finite amplitude disturbances for draw ratios of less than 20.2. Linearized stability analysis revealed that for fluids that obey a White–Metzner-type constitutive equation, the critical draw ratio depends on the Power Law index n and the viscoelastic dimensionless number N

$$N = 3^{(1-s/2)}\left(\frac{m}{G}\right)^{s}\left(\frac{V_0}{L}\right) \tag{14.1-1}$$

where $s = 1/n$, L is the spinline length, G is the tensile modulus, and V_0 is the spinneret velocity. The results appear in Fig. 14.12. Of interest is the ''nose'' region of the curves, which indicates that one could eliminate the draw resonance phenomenon by an *increase* in the draw ratio. Also of interest is the work of Han (37), who finds experimentally that as the temperature level is decreased in isothermal spinning, draw resonance occurs at lower draw ratios. This seems reasonable from the figure. In the ''nose'' region, decreasing the temperature increases G and decreases m, which in turn decreases N, bringing about lower draw ratio values.

White et al. (38,39) presented experimental and theoretical (isothermal linear stability analysis) results that indicate the following: first, that polymer melts respond similarly to uniform elongational flow and to melt spinning; second, that polymers whose elongational viscosity $\bar{\eta}^{+}(t, \dot{\varepsilon})$ increases with time or strain result in a stable spinline, do not exhibit draw resonance, and undergo cohesive failure at high draw ratios. A prime example of such behavior is LDPE. On the other hand, polymer melts with a decreasing $\bar{\eta}^{+}(t, \dot{\varepsilon})$

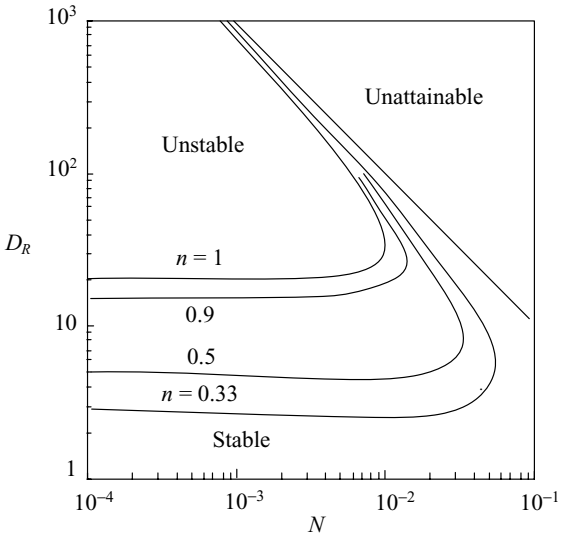

Fig. 14.12 Results of the linearized stability analysis for a White–Metzner-type fluid, indicating the dependence of the critical draw ratio on n and N. [Reprinted by permission from R. J. Fisher and M. M. Denn, ''A Theory of Isothermal Melt Spinning and Draw Resonance,'' *AIChE J.*, **22**, 236 (1976).]

exhibit draw resonance at low draw ratios and break in a ductile fashion (after ''necking'') at high draw ratios. Typical polymers in this category are HDPE and PP.

The preceding analyses were based on steady state solution of the governing equations, and examining the response of the system to applied sinusoidal perturbations. However, for the study of the *dynamics* of the instability, and for tracing the physical sources of instability, transient time-dependent solutions are needed. Hyun et al. (40,41) developed such solutions by tracing and analyzing kinematic traveling waves on the spinline from the spinneret to the take-up. Their simulation shows good agreement with the experiments (28).

14.2 FILM BLOWING

Most films and bags, in sizes varying from a sandwich bag to large films covering building sites, are made by the ingenious and deceptively simple process of film blowing. This process is shown schematically in Fig. 14.13(a), and a photograph of the process is shown in Fig. 14.13(b). A relatively small diameter tubular film is extruded upwards; upon exit it is blown up, with air introduced below the die, into a larger tubular film and then picked up by a pair of nip rolls that seal the bubble. An external stream of chilled air cools and solidifies the film at a certain upstream location called the *freeze line*, where $T_f = T_m$. In this process the film is stretched biaxially, thereby improving its mechanical properties. The blow up ratio, R_f/R_0, determined by the pressure level within the bubble, sets the (tangential) circumferential stretching, and the speed of take-up by the nip rolls sets the axial stretching.

The film thickness produced by film blowing ranges from 10 μm to 100 μm and the rates of production are very high. The most common plastic films produced by this method are branched LDPE, linear low density polyethylene (LLDPE), and linear HDPE films. By using more than one extruder, multilayer films can also be manufactured. To appreciate the

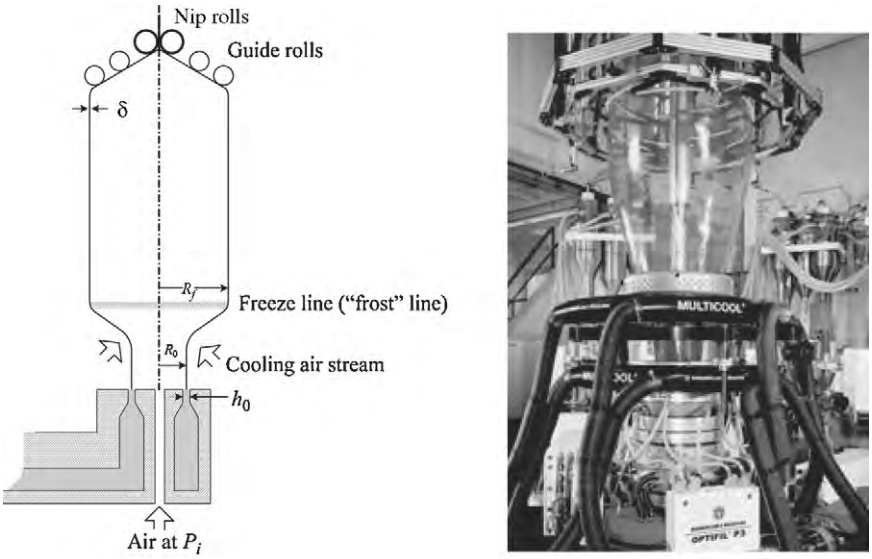

Fig. 14.13 (a) Schematic representation of the tubular blown film forming operation. (b) Photograph of a coextruded blown film die followed by blown film with external and internal cooling. [Courtesy of Windmoeller & Hoelscher (Lincoln RI).]

elegant engineering simplicity of this process, we have to compare it to the more complicated and expensive die forming flat film process, where the melt is extruded through a slit die onto chilled take-up rolls. The latter process, while more expensive, has the advantage of producing optically clear films, because of the profuse nucleation induced by the quenching abilities of the chilled rolls. Yet, as the mathematical analysis discussed below demonstrates, the film blowing process is not simple at all, particularly when we consider the multiplicity of steady states and bubble instabilities that may arise which, in addition to cooling rates, place upper limits on production rates.

The first milestone in modeling the process is credited to Pearson and Petrie (42–44), who laid the mathematical foundation of the thin-film, steady-state, isothermal Newtonian analysis presented below. Petrie (45) simulated the process using either a Newtonian fluid model or an elastic solid model; in the Newtonian case, he inserted the temperature profile obtained experimentally by Ast (46), who was the first to deal with nonisothermal effects and solve the energy equation to account for the temperature-dependent viscosity. Petrie (47) and Pearson (48) provide reviews of these early stages of mathematical foundation for the analysis of film blowing.

Han and Park (49–51) used a coupled force and thermal energy balances to take care of the nonisothermal nature of the process and accounted for the non-Newtonian nature of the viscosity. Gupta (52) presented experimental results that were used by several investigators. Kanai and White (53,54) carried out detailed experimentation as well as theoretical analysis of both the kinematics and the dynamics of the process and the effect of the cooling rate on crystallization. Heat transfer and bubble cooling were studied by Sidiropoulos and Vlachopoulos (55–58), who used numerical simulation to study air flow around the bubble, investigated the effect of internal bubble cooling, and studied the temperature gradient in the blown film. Finally, Campbell et al. (59) carried out a full aerodynamic analysis of the cooling air around the bubble.

The early attempts to account for the viscoelastic nature of the fluid encountered mathematical difficulties in the numerical solutions. Yet later, Luo and Tanner (60) expanded the Petrie model to viscoelastic nonisothermal flow using the convected Maxwell and Leonov (61) models, and compared results to experiments done by Gupta (52). Cain and Denn (62) carried out a detailed analysis of both Newtonian and viscoelastic fluids. For the latter, they used the upper convected Maxwell model and the Marruci (63) model. They found that multiple solutions of the governing equations are possible even for the Newtonian fluid, with the existence of more than one steady state bubble profile for a given set of operating conditions. Furthermore, they found several types of instabilities. A recent, detailed review of film blowing instabilities is given by Jung and Hyun (28).

Following the principles of the Petrie model, and recalling that the film thickness δ is much smaller than the radius $\delta/R \ll 1$, we invoke the ''thin-film approximation,'' which implies that field equations are averaged over the thickness and that there are no shear stresses and moments in the film. The film is regarded, in fact, as a thin shell in tension, which is supported by the longitudinal force F_z in the bubble and by the pressure difference between the inner and outer surfaces, ΔP. We further assume steady state, a clearly defined sharp freeze line above which no more deformation takes place and an axisymmetric bubble. Bubble properties can therefore be expressed in terms of a single independent spatial variable, the (upward) axial position from the die exit,[2] z. The object

2. To be exact, the origin of variable z is located not at the die exit, but just past the die-exit swell region (21).

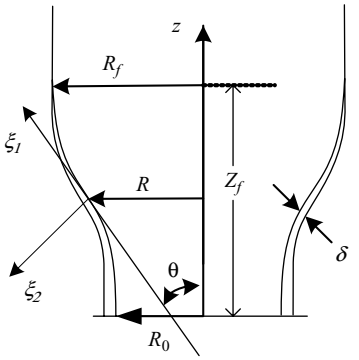

Fig. 14.14 The melt exits the die at $z = 0$; the radius of the bubble R and the thickness δ are a function of z. The coordinate system ξ_i is embedded into the inner surface of the bubble.

of the analysis is to predict the dependent variables, including the bubble radius, film thickness, film temperature (in the nonisothermal case), and local values of stresses as a function of the axial distance, z.

We first derive the kinematics of the deformation. The flow situation is shown in Fig. 14.14. Coordinate z is the vertical distance in the center of the axisymmetric bubble with the film emerging from the die at $z = 0$. The radius of the bubble R and its thickness δ are a function of z. We chose a coordinate system ξ_i embedded in the inner surface of the bubble. We discussed extensional flows in Section 3.1 where we defined the velocity field of extensional flows as

$$v_i = a_i \xi_i \tag{14.2-1}$$

In this case, as pointed out earlier, the extension is planar, but unequal in directions ξ_1 and ξ_3. In order to derive the rate of deformation tensor components, we need to define the flow field in terms of the dependent variables δ and R. We note that in direction "2" at $\xi_2 = \delta$, we can write

$$v_2 = a_2 \delta = \frac{d\delta}{dt} \tag{14.2-2}$$

Writing a_2 in terms of δ, from the kinematics of extensional flow, we have

$$\dot{\gamma}_{22} = 2a_2 = \frac{2}{\delta}\frac{d\delta}{dt} \tag{14.2-3}$$

We can rewrite Eq. 14.2-3 as follows

$$\dot{\gamma}_{22} = 2a_2 = \frac{2}{\delta}\frac{d\delta}{d\xi_1}\frac{d\xi_1}{dt} \tag{14.2-4}$$

where

$$\frac{d\xi_1}{dt} = v_1 \tag{14.2-5}$$

And from geometrical considerations, we find that

$$\frac{d\delta}{d\xi_1} = \frac{d\delta}{dz}\frac{dz}{d\xi_1} = \cos\theta\frac{d\delta}{dz} \tag{14.2-6}$$

Substituting Eqs, 14.2-6 and 14.2-5 into Eq. 14.2-4, we get

$$\dot{\gamma}_{22} = \frac{2}{\delta}v_1\cos\theta\frac{d\delta}{dz} \tag{14.2-7}$$

The volumetric flow rate Q is given by

$$Q = 2\pi R\delta v_1 \tag{14.2-8}$$

Substituting it into Eq. 14.2-7, we obtain

$$\dot{\gamma}_{22} = \left(\frac{Q\cos\theta}{\pi R\delta}\right)\frac{1}{\delta}\frac{d\delta}{dz} \tag{14.2-9}$$

The film circumference at any given z where the bubble radius is R, is $l = 2\pi R$, and the velocity v_3 is given by

$$v_3 = \frac{dl}{dt} = 2\pi\frac{dR}{dt} = 2\pi\frac{dR}{d\xi_1}\frac{d\xi_1}{dt} \tag{14.2-10}$$

Substituting Eq. 14.2-5 into Eq.14.2-10 and recalling that $dz/d\xi_1 = \cos\theta$, we get

$$v_3 = 2\pi v_1\cos\theta\frac{dR}{dz} \tag{14.2-11}$$

Next we substitute Eq. 14.2-8 into Eq.14.2-11 and with Eq. 14.2-1, get

$$v_3 = \frac{Q\cos\theta}{\delta}\frac{1}{R}\frac{dR}{dz} = 2\pi R a_3 \tag{14.2-12}$$

Recalling that $\dot{\gamma}_{33} = 2a_3$, we obtain

$$\dot{\gamma}_{33} = \left(\frac{Q\cos\theta}{\pi R\delta}\right)\frac{1}{R}\frac{dR}{dz} \tag{14.2-13}$$

Finally, we obtain the third component of the rate of deformation tensor $\dot{\gamma}_{11}$ from the equation of continuity $\Sigma a_i = 0$ or $\Sigma\dot{\gamma}_{ii} = 0$ to give

$$\dot{\gamma}_{11} = -\frac{Q\cos\theta}{\pi R\delta}\left(\frac{1}{\delta}\frac{d\delta}{dz} + \frac{1}{R}\frac{dR}{dz}\right) \tag{14.2-14}$$

Having the components of the rate of deformation tensor, we can turn to the components of the stress tensor assuming a Newtonian fluid

$$\boldsymbol{\pi} = P\boldsymbol{\delta} - \mu\dot{\boldsymbol{\gamma}} \tag{14.2-15}$$

Setting $\pi_{22} = 0$ because no external forces act in this direction, we can extract P from the previous equation after substituting Eq. 14.2-9, to obtain

$$P = \frac{\mu Q \cos\theta}{\pi R\delta^2}\frac{d\theta}{dz} \tag{14.2-16}$$

From the foregoing, the two other normal stress components can be evaluated

$$\pi_{11} = \frac{Q\mu\cos\theta}{\pi R\delta}\left(\frac{2}{\delta}\frac{d\theta}{dz} + \frac{1}{R}\frac{dR}{dz}\right) \tag{14.2-17}$$

$$\pi_{33} = \frac{Q\mu\cos\theta}{\pi R\delta}\left(\frac{1}{\delta}\frac{d\theta}{dz} - \frac{1}{R}\frac{dR}{dz}\right) \tag{14.2-18}$$

To solve for $\delta(z)$ and $R(z)$, one needs to state the force balance equations for the blown film. The simplest form of these equations, disregarding inertial and gravity forces, are the classic thin-film equations. The forces per unit length in the film in the ξ_1 and ξ_3 directions are $F_L/2\pi R = \delta\pi_{11}$ and $F_H/\xi_1 = \delta\pi_{33}$, respectively; thus from the thin film equation, we get

$$\Delta P = -\delta\left(\frac{\pi_{11}}{R_L} + \frac{\pi_{33}}{R_C}\right) \tag{14.2-19}$$

where $R_C = R\sqrt{1+\dot{R}^2} = R/\cos\theta$ and $R_L = -(1+\dot{R}^2)^{3/2}/\ddot{R} = -\sec^3\theta/\ddot{R}$ are the radii of curvature with $\dot{R} = dR/dz$ and $\ddot{R} = d\dot{R}/dz$. Next we make a force balance in the z direction on a portion of the bubble bound by two planes, one at z and the other at the freeze line $z = Z_F$, where the radius is R_F, and the force F_z, acting in the axial direction on the bubble for $z \geq Z_F$, is

$$F_z = -(2\pi R\cos\theta)\delta\pi_{11} + \pi\Delta P(R_f^2 - R^2) \tag{14.2-20}$$

By substituting Eq. 14.2-17 and 14.2-18 into Eqs. 14.2-19 and 14.2-21, we obtain two differential equations, one for the radius and the other for the thickness. In terms of the dimensionless parameters $r = R/R_0$, $w = \delta/R$, and $\zeta = z/R_0$

$$2r^2(A + r^2B)\ddot{r} = 6\dot{r} + r(1+\dot{r}^2)(A - 3r^2B) \tag{14.2-21}$$

where $\dot{r} = dr/d\zeta$ and $\ddot{r} = d\dot{r}/d\zeta$, and is subject to boundary conditions $r(0) = 1$ and $\dot{r}\,(\zeta_f) = 0$, and

$$\dot{w} = -w\left[\frac{\dot{r}}{2r} + \frac{(1+\dot{r}^2)(A + r^2B)}{4}\right] \tag{14.2-22}$$

where $\dot{w} = dw/d\zeta$, and dimensionless groups A and B are

$$A = \frac{R_0 F_z}{\mu Q} - B\left(\frac{R_f}{R_0}\right)^2 \tag{14.2-23}$$

$$B = \frac{\pi R_0^3 \Delta P}{\mu Q} \tag{14.2-24}$$

subject to boundary conditions $w(0) = \delta_0/R_0$.

Note that in order to solve these equations, the position of the freeze line Z_f and the value δ_0 at the die exit (post–die exit swelling) must be known. Neither quantity can be specified a priori. Cain and Denn (62) discuss the numerical solution of these equations for various rheological models. The two differential equations are decoupled, and after solving Eq. 14.2-22 for the radius profile, which most investigators solve by using a fourth-order Runge–Kutta method, the results can be inserted into Eq. 14.2-22 to obtain the thickness profile. In the former, a final bubble radius at the freeze line is assumed and the initial bubble radius at the origin is computed. Then the freeze-line radius is adjusted until the desired initial radius is achieved. Cain and Denn simulations, using the rich experimental data collected by Gupta (52), show a complex, multiple, steady state behavior even for the Newtonian isothermal model. Han and Park (50) carried out LDPE film blowing experiments and, using a modified model described earlier with a Power Law–type temperature-dependent viscosity and heat transfer calculation, showed good agreement between simulation and experiments (64).

Bubble instability is one of the complications of this process. Only recently did this matter receive theoretical attention. As pointed out by Jung and Hyun (28), there are three characteristic bubble instabilities: axisymmetric draw resonance, helical instability, and metastability where the bubble alternates between steady states, and the freeze line moves from one position to another. Using linear stability analysis, Cain and Denn (62) showed that multiple steady state solutions are possible for the same set of conditions, as pointed out earlier. However, in order to study the dynamic or time-dependent changes of the process, transient solutions are needed. This was recently achieved by Hyun et al. (65), who succeeded in quite accurately simulating the experimentally observed draw resonance (28).

14.3 BLOW MOLDING

Blow molding is a very important polymer processing method, borrowed from the glass industry, for manufacturing hollow articles such as small bottles for household products and personal care, dairy products and beverages, containers for industrial goods or chemicals, fuel tanks, drums, car dashboards, and so on (66–68). There are three basic types of blow molding processes: *extrusion*, *injection*, and *stretch blow molding*. Classic extrusion blow molding involves first the forming of a molten tube, called the *parison.* The parison is engaged between two mold halves and, upon their closing, is inflated like a balloon by compressed air, to conform to the interior shape of the chilled mold, as shown in Fig. 14.15. The polymer quickly solidifies upon contact with the cold mold, and the finished hollow article is ejected.

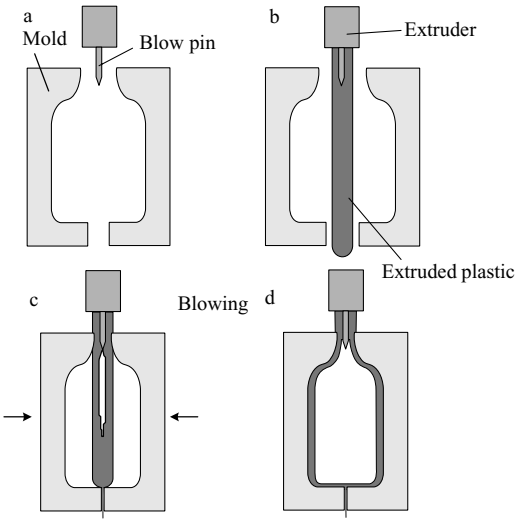

Fig. 14.15 Schematic representation of the blow molding process. (a) The extruder head with the blowing pin and open mold; (b) the extrusion of the parison; (c) the mold closed with the parison pinched in the bottom and sealed at the top; (d) the inflated parison forming a bottle.

The *extrusion blow molding* process can be continuous or intermittent, as shown in Fig. 14.16. The former, employed commonly for parts less than 1 gal, has a continuously rotating screw extruder, extruding parisons through one or more dies. The latter may use either an accumulator head with a piston-driven extrusion forming of the parison, or a reciprocating screw, such as the one used in injection molding.

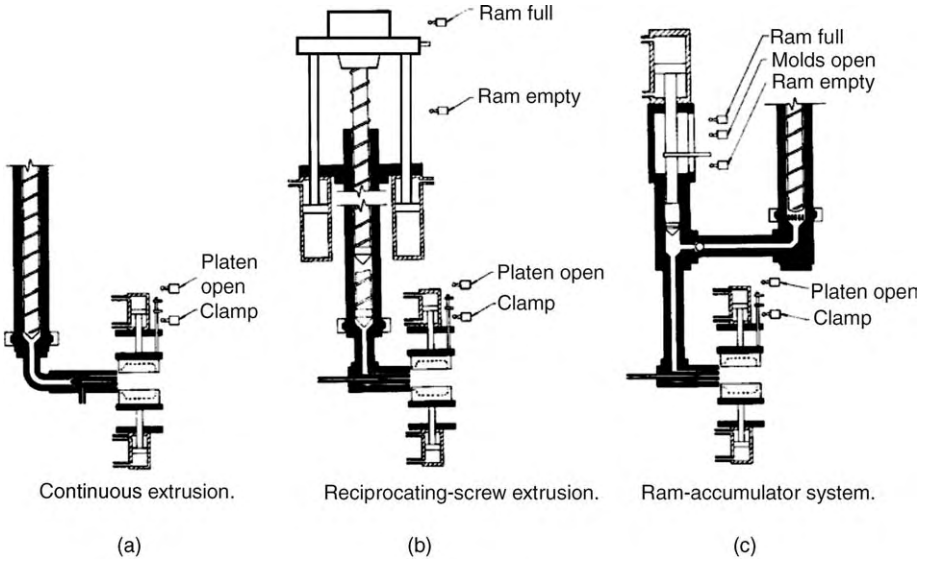

Fig. 14.16 Schematic view of (a) continuous extrusion blow molding; (b) reciprocating screw blow molding; and (c) ram-accumulator blow molding. [Reprinted by permission from *Modern Plastics Encyclopedia*, McGraw-Hill, New York, 1976–1977.)

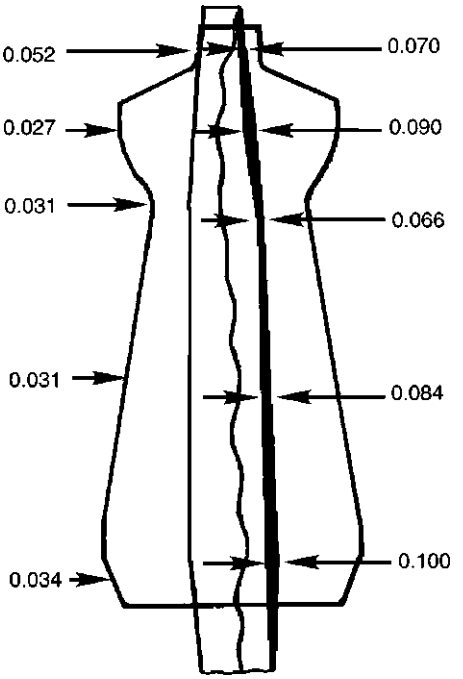

Fig. 14.17 Example of a parison thickness variation by parson "programming." [Reprinted by permission from *Modern Plastics Encyclopedia*, Vol. 53, McGraw-Hill, New York, 1976–1977.]

The intermittent-parison production methods are more suited to the nature of the blow molding process; greater flexibility and control are possible in the forming itself, which is the heart of the process. The inflation step is fast, and little flexibility is allowed in the control of the "bubble" thickness. Thus, by controlling the rate of extrusion during parison forming (which results in different degrees of swelling of the extrudate), the thickness of the parison can be programmed to result in a product of more-or-less uniform thickness. Figure 14.17 shows a parison of programmed thickness. The same result can be obtained by varying the annular die gap and extruding the polymer at a constant rate. Parison forming is very sensitive to both shear and extentional rheological properties, hence to temperature.

It is possible to blow mold several layers of material by coextrusion blow molding processes. By appropriate material selection, the various parts of the structure can be optimized for the best balance between properties and cost.

In the *injection blow molding* process, the parison is formed by injection molding of the preshaped parison onto a steel rod, as shown in Fig. 14.18. The rod with the molded thread already completed is moved to the blowing station, where the article is inflated free of scrap. The parison thickness distribution is determined in the injection mold without the need of further control. Some axial orientation is introduced during injection, resulting in an article with partial biaxial orientation.

A process that greatly improves blow molded product properties is that of *injection stretch blow molding*, which introduces biaxial orientation in crystallizable polymers. There are two variants of this process involving the molding of a preform as the first step. The thermomechanical paths of the two process variants are shown in Fig. 14.19. In the

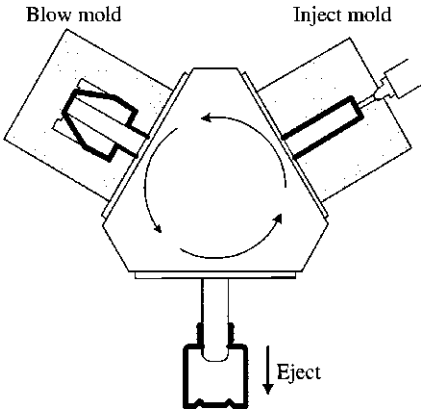

Fig. 14.18 Schematic of the three-position injection blow-molding rotary machine. The third position is easily accessible for removing the blow-molded article. [Reprinted by permission from *Modern Plastics Encyclopedia*, Vol. 53, McGraw-Hill, New York, 1976–1977.]

two-step process, the preform is molded, cooled and transported to the stretch blow molding station, where it is *reheated* (thermally conditioned) to a temperature, T_s, above T_g, but well below T_m, and stretched with an axially moving rod, while simultaneously being blown in a mold. In the one-step process the preform is *cooled* to the stretching temperature T_s, and then is stretched and blown in the same molding station to conform in shape with the mold. Although thermally efficient, the one-step process is not process efficient, since it ties up the equipment during the parison cooling time period, which cannot be very small, since a preformwide uniform temperature must be attained before

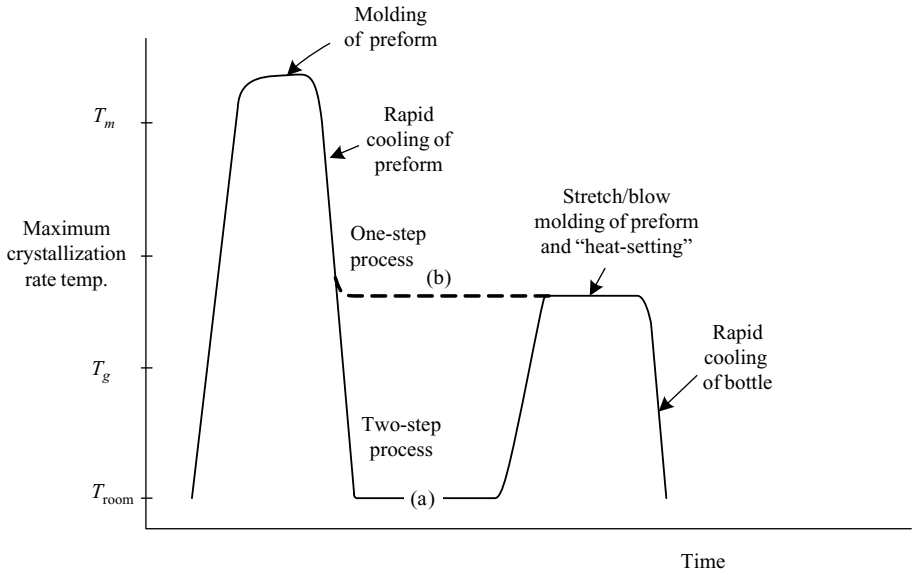

Fig. 14.19 Thermomechanical histories of the two variants of the injection stretch blow molding process; (a) the two-step, and (b) the less common one-step.

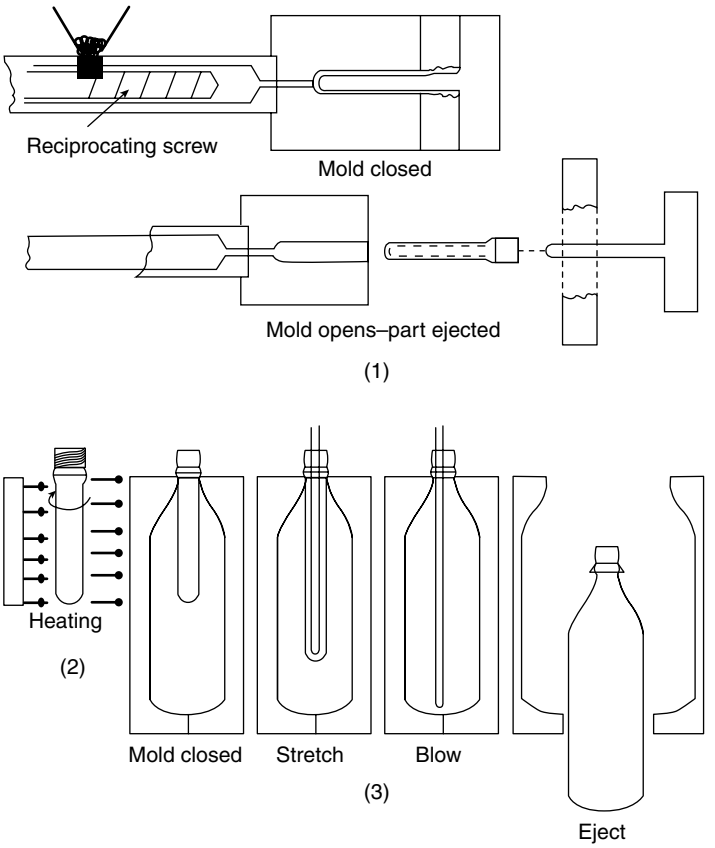

Fig. 14.20 Schematic representation of the injection stretch blow-molding process. Step (1) producing preforms may be carried out in different location from the stretch blow molding process. [Reprinted by permission from Schmidt et al., ''Experimental Study and Numerical Simulation of the Injection Stretch/Blow Molding Process,'' *Polym. Eng. Sci.*, **38**, 1399 (1998).]

the stretching and blowing step. Thus, the two-step process is the most common and is typically used to produce PET carbonated beverage bottles, which represent a very large volume market. The stages of the two-step process are shown in Fig. 14.20. The reason for thermally conditioning the preform in both process variants to the previously given temperature range, $T_g < T_s < T_m$, is to *allow for crystallization* during the biaxial stretch blow molding step, as shown in Fig. 14.21. In this way, deformation-induced crystallization is promoted *both* during the stretch blow molding stage and the heat-setting stage, if a hot mold is used. Following Druin (68), standard PET carbonated beverage bottles are produced by heating the preform to 95°–105°C and stretch blow molding it into a cold mold (3°–10°C), producing a deformation-induced crystallinity of 25%. The resulting product T_g is 73°C, and the O_2 and CO_2 permeability is reduced to half that of an nonoriented amorphous PET film.

If the preheated preform is stretched and blown into a *hot* mold, for example, 100–110°C and held there for a short period, the resulting T_g is in the range of 88°C, allowing for ''hot fill'' capabilities of such bottles, increasing the crystallinity to the 28–30% level and further decreasing the O_2 permeability to one-third that of an nonoriented amorphous

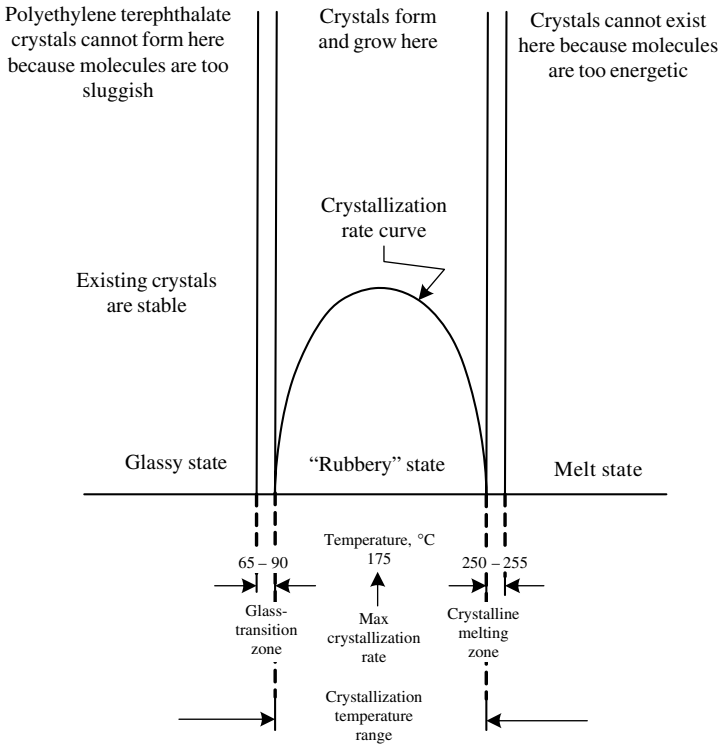

Fig. 14.21 Schematic representation of the crystallization behavior of PET relative to the stretch blow molding process. [J. S. Schaul, ''Drying and Injection Molding PET for Beverage Bottle Preform,'' *SPE ANTEC Tech. Papers,* **26**, 534 (1980).]

PET film. The overall improvement in ''barrier'' properties of PET upon biaxial deformation, followed by heat-setting, is the *combined* result of higher deformation-induced crystallization and orientation. The role of crystallinity may be more significant than that of orientation, because it reduces both the diffusion rate (increasing the permeant's path ''tortuosity'') as well as its solubility, while orientation reduces only the diffusion rate.

Figure 14.22 plots the oxygen permeability of PET nonoriented sheets and biaxially oriented bottles as a function of the degree of crystallinity. Indeed, the effect of crystallinity is larger than that of biaxial orientation. But in practical terms, nonoriented sheets crystallize much more slowly than the biaxially oriented bottle walls, because deformation-induced orientation proceeds at higher rates at any temperature between T_g and T_m. That is, the schematically represented ''crystallization rate'' curve in Fig. 14.21 extends vertically upwards.

The real ''structuring'' benefit, then, of the stretch blow molding–induced biaxial deformation is to create the needed degree of crystallinity during the very short stretch blowing and heat-setting times, which makes the process commercially viable. Finally, the deformation-induced nonspherulitic crystalline morphology not only increases the modulus of elasticity, but also the impact strength of the stretch blow molded bottles. Thus, the structuring achieved during stretch blow molding for plastic materials has opened up the vast market for bottling pressurized supersaturated carbonated drinks, at

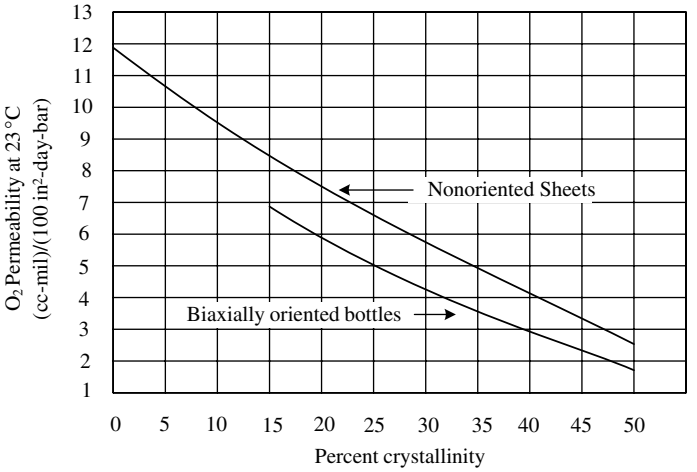

Fig. 14.22 Oxygen permeability of nonoriented PET sheets and biaxially oriented PET bottles as a function of crystallinity. [M. Salame, paper presented at the *Bev-Pak 1992 Conference*, Atlanta, GA March 23–25 (1992).]

the expense of both glass and aluminum containers, which have product-appropriate strength (though glass is brittle and thus breakable) and permeability, but are costlier to fabricate.

Finally, it is worth mentioning the more recent three-dimensional blow molding in which a robot arm optimally positions the parison in the mold cavity, to minimize trim-off, and to produce complex shapes, such as automotive parts.

Parison Formation

If the ratio of the final postinflation diameter to parison diameter is constant along the parison length (cylindrical shape), then the parison thickness should be uniform along its length. If, however, it varies, the parison should be thicker at axial locations where the diameter ratio is larger. Only under such conditions can acceptable product strength levels be reached with minimum product weight. To accomplish thickness control of the parison, special dies have been designed. In a typical reciprocating screw blow molding die head (Fig. 14.23), the choke screw D is adjustable to compensate for batch-to-batch or polymer-to-polymer viscosity variations. The choke ring I is adjustable to eliminate circumferential melt pressure variations. It also forms an annular channel that is narrow enough to ensure reduction of the effects of the varying melt flow histories of the incoming melt. The centering screw J is used for the final adjustments, which ensure that there is no angular dependence of the parison thickness or diameter.

The final die gap is a conical section, slightly tapering, annular channel. The cone angle Θ is appreciable (Fig. 14.24) and is an important die design variable in determining the parison diameter, diameter profile, and thickness. Furthermore, an angle $\theta > 0$ allows convenient die gap adjustment through slight axial mandrel position changes.

Figure 4.25 shows other possible parison die designs: diverging, converging, and straight, that also allow for flow rate control. An appreciable value of the diverging or converging angle renders the flow in the conical die land gap nonviscometric, consisting of both shear and planar extensional flows. This makes extrudate swell prediction

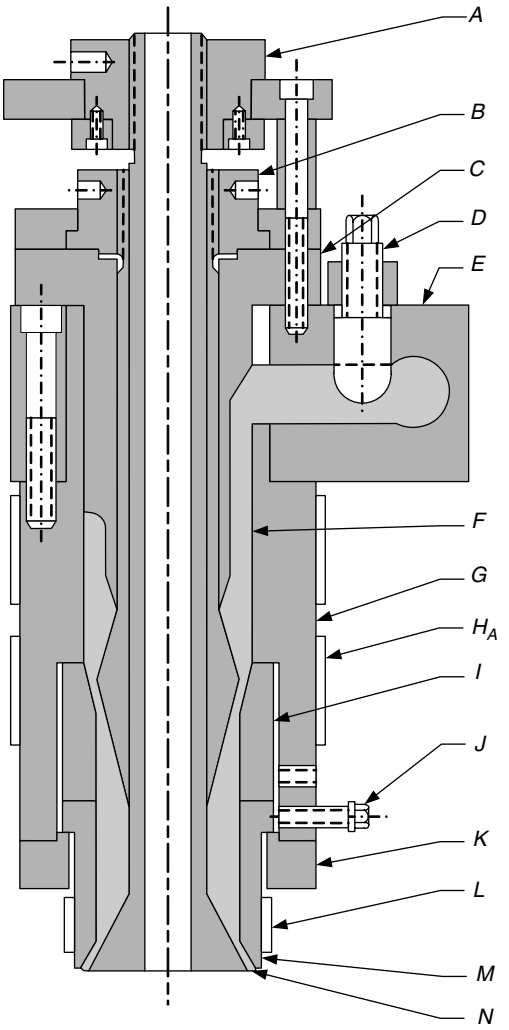

Fig. 14.23 Typical blow molding die: *A*, choke adjusting nut; *B*, mandrel adjustment; *C*, feed throat; *D*, choke screw; *E*, die head; *F*, plastic melt; *G*, die barrel; *H*, heater band; *I*, choke ring; *J*, centering screw; *K*, clamp ring; *L*, die heater; *M*, die; *N*, mandrel. [Reprinted by permission from J. D. Frankland, "A High Speed Blow Molding Process," *Trans. Soc. Rheol.*, **19**, 371 (1975).]

more difficult, in particular since the polymers that are suitable for the blow molding process are generally strongly elastic with a high extensional viscosity to avoid parison sagging and to undergo stable parison blowing to form final products. Moreover, in annular extrudate swell, in addition to the thickness swell (equivalent to radial swell in capillary flow), we must also deal with the diameter swell, as indicated in Fig. 14.18, both of which are affected by sagging due to gravitational forces; hence they are time-dependent and also affected by nonuniform temperature due to cooling of the parison. It is not surprising, therefore, that numerical methods are still somewhat limited, and semiempirical methods based on experimental measurements need to be used in process and die design.

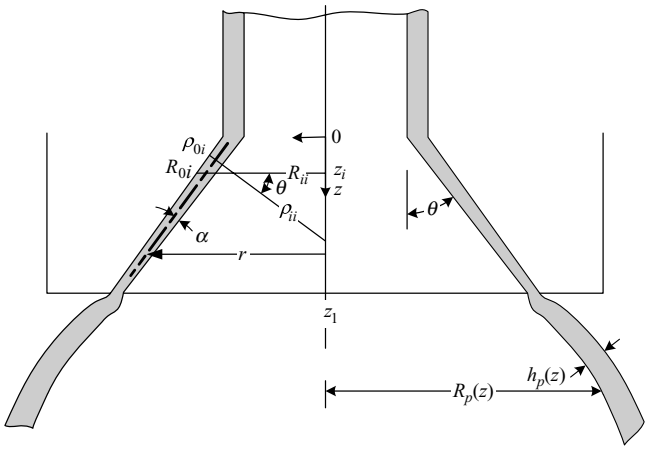

Fig. 14.24 Detailed cross-sectional representation of the die exit and the parison formed in the blow molding process, with the key design variables and the thickness and outer diameter swell.

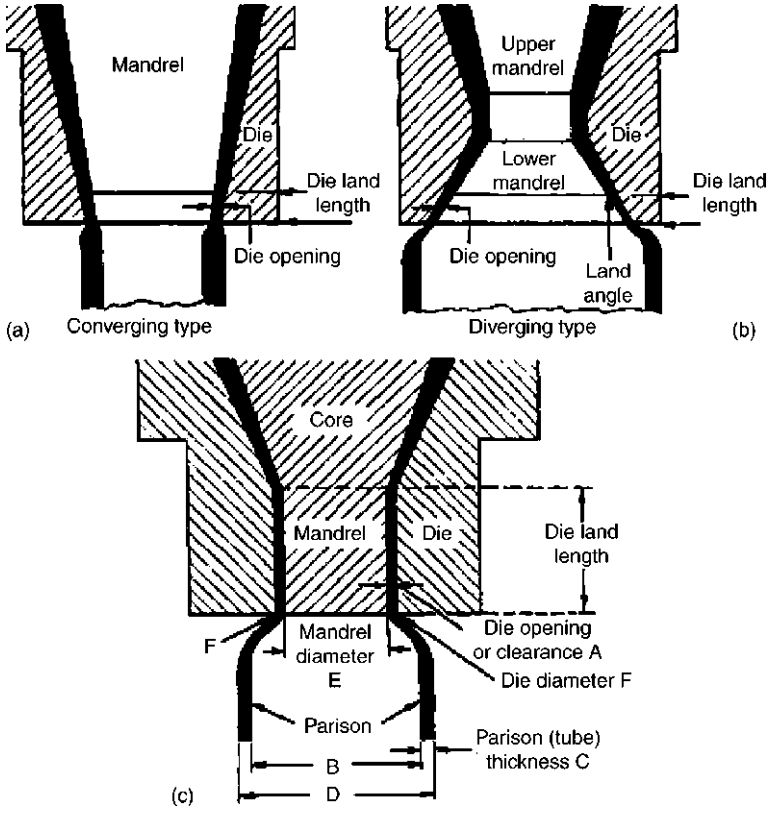

Fig. 14.25 Schematic parison die designs: (a) convergent; (b) divergent, and (c) straight. [Reprinted by permission from A. Gracia-Rejon, R. W. DiRaddo, and M. E. Ryan, "Effect of Die Geometry and Flow Characteristics on Viscoelastic Annular Die Swell," *J. Non-Newt. Fluid Mech.*, **60**, 107–128 (1995).]

A simple and straightforward experimental method to determine parison shape and thickness distribution was suggested by Sheptak and Beyer (69), who developed a mold that pinched off the extruded parison in several axial segments, enabling the measurement of the weight and the lay-flat width of each segment. Kamal et al. (70) derived a time-dependent relationship between diameter and thickness swell based on experimental data. Kamal and Kalyon (71) correlated between area swell and capillary swell. Gracia-Rejon et al. (72) explored the effect of the die geometry (e.g., diverging versus converging, die contraction ratio, inclination angle, and length of tapered section) and flow characteristic on viscoelastic annular swell of HDPE using the commercial POLYFLOW FEM program and the Kaye-Bernstein-Kearrsley-Zappas (K-BKZ) constitutive model. They found that diameter and thickness swell depend on the extent of elongational and shear deformation history in the die and, of course, the rheological characteristics of the polymer. Orbey and Dealy (73) also explored the effect of die design on annular swell values for both converging and diverging dies, and they (74) developed a lumped parameter model to predict the length and shape of the parison on the basis of experimental swell data and storage modulus of the resin. Wagner and Kalyon (75) studied parison shape and thickness distribution experimentally using cinematography and a transparent mold with a range of polyamide resins. They observe differences in behavior that cannot be easily related to the rheological properties of the resins. As Fig. 14.26(a), 14.26(b), and 14.26(c) indicates there are great differences in swell behavior between the resins. The straight nylon [Fig. 14.26(a)] shows greater nonuniformity along the axis. Diameter swell increases from 1.1 to 1.3, whereas the weight and thickness swell undergo a minimum, due to drawdown or sag and strain recovery. The addition of 12% glass fiber significantly reduces swell, with diameter swell slightly above 1 and the weight and thickness swell below 1 due to drawdown, this, in spite of measuring similar primary normal stress difference and storage modulus for the two resins. The polyolefin modified resin shows the largest swell ratio and minimal drawdown, indicating higher melt strength resisting drawdown.

Laroche et al. (76), who developed an integrated numerical model for the blow molding process, observe that computation of the annular die swell using differential viscoelastic constitutive models were found to overpredict the measured swell levels. Integral constitutive models, such as the K-BKZ constitutive equation, have proved to be more reliable. They deal with parison formation by a numerical Lagrangian scheme, whereby the parison is subdivided into axial increments and followed from emergence from the die to the end of the cycle. In each one, deformation due to swell and sagging is obtained using empirical relations.

Tanue et al. of the Funatsu computational group (77) using an FEM formulation and a Giesekus constitutive model (17), predicted the parison swell and shape within 20% accuracy, though it appears that they neglected gravitational effects. A number of viscoelastic constitutive equations (e.g., K-BKZ, Larson) for computing HDPE annular extrudate swell in large parisons were explored by Otsuki et al. of the same group (78), indicating very different responses with the different models, and great sensitivity to differences in resin properties at relatively small deformation.

The SIMBLOW[3] integrated FEM simulation commercial software for the extrusion blow molding process also uses the K-BKZ fluid (79), which accounts for shear thinning,

3. The Plamedia Research Corporation (Tokyo, Japan)

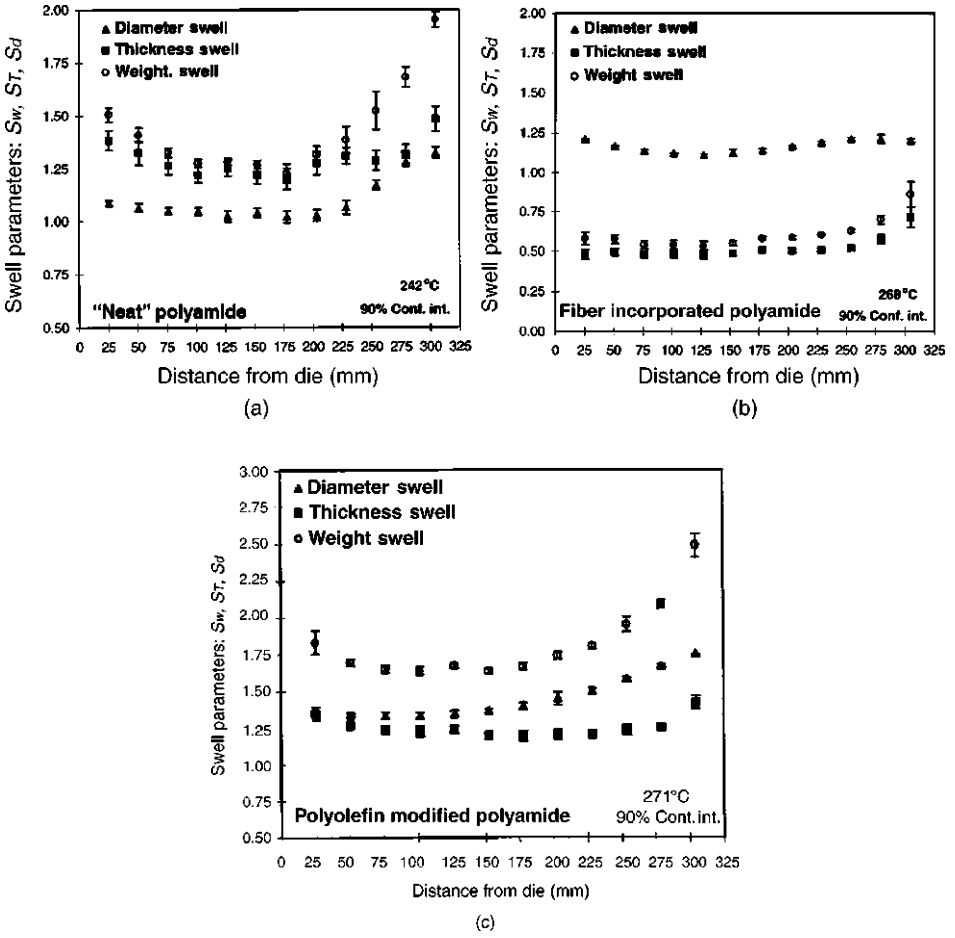

Fig. 14.26 Diameter (S_D, thickness (S_T), and weight (S_W) swell of a parison extrudate from a commercial blow-molding machine equipped with CCD camera equipment and parison pinch-off mold based on the design of Shepak and Beyer (69). (a) A chain extended multibranched polyamide-6 resin; (b) the former with 12% glass fiber of 10 μm diameter 60:1 L/D; and (c) polyolefin modified polyamide-6 with some carbon black. [Reprinted by permission from A. H. Wagner and D. Kalyon, "Parison Formation and Inflation Behavior pf Polyamide-6 During Extrusion Blow Molding," *Polym. Eng. Sci.*, **36**, 1897–1906 (1996).]

normal stresses in shear flow, and elastic behavior. It is a special case of the Lodge rubber-like liquid constitutive equations (Eqs. 3.4-4 and 3.4-5)

$$\boldsymbol{\tau}(t) = \int_{-\infty}^{t} \left[\sum_i G_i \exp\left(-\frac{t-t'}{\lambda_i} \right) h(\gamma)[\boldsymbol{\gamma}[1](t',t), -\mathbf{I}] \right] dt' \tag{14.3-1}$$

where $\boldsymbol{\gamma}[1]$ is the Finger tensor and H_t is the dynamic damping function to account for nonlinearity in the relaxation spectrum (G_i, λ_i) (80). The evaluation of the material rheological parameters needed in Eq.14.3-1 requires the following characterization experiments: dynamic mechanical, steady shear, and transient uniaxial elongational flow.

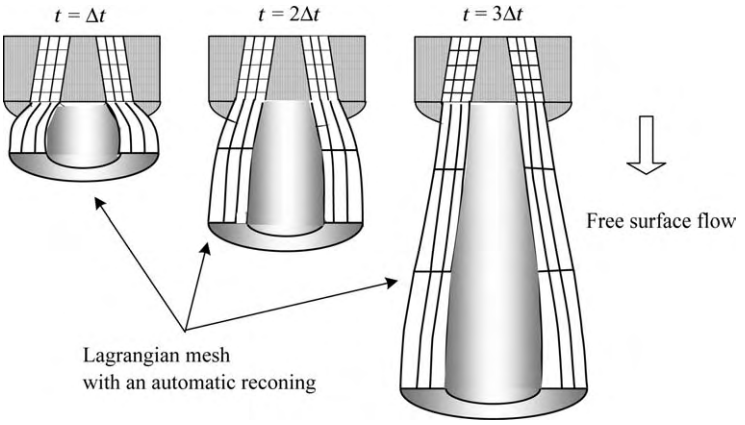

Fig. 14.27 Lagrangian mesh used in the FEM in the post–die extruded parison. [Reprinted by permission from the Plamedia Research Corporation, Tokyo, Japan.]

The momentum and energy equations are then cast in an Eulerian FEM mesh inside the conical die and a Lagrangian mesh in the parison being formed, as shown in Fig. 14.27. Typical results obtained with SIMBLOW are depicted qualitatively in Fig. 14.28. A conical parison is formed initially, which, under the body force of gravity, turns vertical downwards. The gradual thickening of the parison is due to the axial programmed parison core movement.

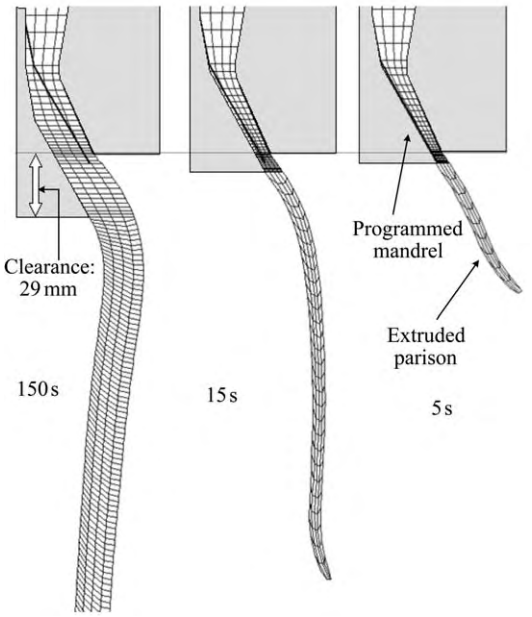

Fig. 14.28 Parison shape and thickness profile of the parison at different times with programmed mandrel and a region of partially confined extrudate. [Reprinted by permission from the Plamedia Research Corporation, Tokyo, Japan.]

Parison Inflation

The parison is inflated fast, within seconds or less, at a predetermined rate such that it does not burst while expanding. It is a complex process that involves expansion of a nonuniform membrane-like element. Because the extension ratio is high (above 10), it is difficult to calculate the final thickness distribution. Naturally, much of the recent theoretical research on parison stretching and inflation (as in the case with thermoforming) focuses on FEM methods and the selection of the appropriate rheological constitutive models to predict parison shape, thickness, and temperature distribution during the inflation.

FEM is the only practical tool to handle the problem. Not surprisingly, this method was first applied to membranes or thin shells in the field of structural analysis, a field where, in fact, FEM was pioneered, with a much later penetration to fluid mechanics and polymer processing. Indeed, Oden and Sato (81) were the first to apply FEM to examine the three-dimensional membrane inflation problem. Two other engineering fields that apply a similar FEM approach are metal sheet forming and glass bottle blowing (82).

Parison inflation models use a Lagrangian framework with most of them employing the thin-shell formulation and various solidlike or liquid constitutive equations, generally assuming no-slip upon the parison contacting the mold. The first attempts to simulate polymeric parison inflation were made by Denson (83), who analyzed the implications of elongational flow in various fabrication methods, as discussed in the following example.

Example 14.2 Inflation of a Cylindrical Uniform Parison Assuming Simple Planar Extensional Flow Following Denson (83), an approximate description of the inflation of a cylindrical parison of uniform radius R_i and thickness h_i to that R_0 and h_0 can be obtained by assuming that (a) the flow is a planar extension; (b) the flow is isothermal; and (c) $h/r \ll 1$, so that the hoop stress $\tau = -[PR(t)/h(t)]$. Experimentally, planar extensional viscosity at very low strain rates (which clearly is a poor approximation for blow molding processes) can be expressed as

$$\bar{\eta}_{pl} = K(\dot{\varepsilon}_{pl})^{n-1} \tag{E14.2-1}$$

The tangential elongational stress component $\tau_{\theta\theta}$ is given by

$$\tau_{\theta\theta} = -\frac{PR(t)}{h(t)} = -K(\dot{\varepsilon}_{pl})^{n-1}\dot{\varepsilon}_{pl} \tag{E14.2-2}$$

Since

$$\dot{\varepsilon}_{pl} = \frac{1}{R(t)}\frac{dR(t)}{dt} \tag{E14.2-3}$$

and for an incompressible material we have

$$V = 2\pi R(t)h(t)L = \text{const.} \tag{E14.2-4}$$

we obtain the expression

$$\frac{dR}{dt} = CP^s R^{2s+1} \tag{E14.2-5}$$

where $s = 1/n$ and

$$C = \left(\frac{2\pi L}{VK}\right)^s \tag{E14.2-6}$$

Equation E14.2-5 can be solved for any time-dependent or constant inflation pressure to give the radial value as a function of time. For example, if P is constant, the parison inflation time is

$$t = \frac{1}{2sCP^s}\left[\left(\frac{1}{R_i}\right)^{2s} - \left(\frac{1}{R_0}\right)^{2s}\right] \tag{E14.2-7}$$

However, since extentional viscous flow behavior is expected to occur only below a certain critical strain rate given by $\dot{\varepsilon} = (2\lambda_{\max})^{-1}$, and the blow-molding inflation rates are high, the preceding approximation may only hold at high temperatures, where the maximum relation time is small.

Petrie and Ito (84) used numerical methods to analyze the dynamic deformation of axisymmetric cylindrical HDPE parisons and estimate final thickness. One of the early and important contributions to parison inflation simulation came from DeLorenzi et al. (85–89), who studied thermoforming and isothermal and nonisothermal parison inflation with both two- and three-dimensional formulation, using FEM with a hyperelastic, solidlike constitutive model. Hyperelastic constitutive models (i.e., models that account for the strains that go beyond the linear elastic into the nonlinear elastic region) were also used, among others, by Charrier (90) and by Marckmann et al. (91), who developed a three-dimensional dynamic FEM procedure using a nonlinear hyperelastic Mooney–Rivlin membrane, and who also used a viscoelastic model (92). However, as was pointed out by Laroche et al. (93), hyperelastic constitutive equations do not allow for time dependence and strain-rate dependence. Thus, their assumption of quasi–static equilibrium during parison inflation, and overpredicts stresses because they cannot account for stress relaxation; furthermore, the solutions are prone to numerical instabilities. Hyperelastic models like viscoplastic models do allow for strain hardening, however, which is a very important element of the actual inflation process.

Vantal et al. (94) and Rodriguez-Villa et al. (95) used viscoplastic models. Wang et al. (96) also used a viscoplastic model, but assumed the material's behavior at elevated temperatures to be strain-rate-dependent, and a non-Newtonian creeping material model to specify the strain rate–sensitive characteristic of the material, strain hardening, and temperature dependence. They applied the model to PET stretch blow molding, and simulated three cases: inflation without stretching, stretching followed by inflation, and simultaneous stretching and inflation. Their conclusion is that the first case cannot be used to produce a real product, the second case can lead to wrinkling, and only the third case resulted in stable and smooth deformation.

With viscoelastic models used by an increasing number of researchers, time and temperature dependence, as well as strain hardening and nonisotropic properties of the deformed parison can, in principle, be accounted for. Kouba and Vlachopoulos (97) used the K-BKZ viscoelastic constitutive equation to model both thermoforming and parison membrane stretching using two-dimensional plate elements in three-dimensional space. Debbaut et al. (98,99) performed nonisothermal simulations using the Giesekus constitutive equation.

Shrivastava and Tang (100) used a viscoelastic constitutive equation with special reference to thermoforming, whereas Laroche et al. (101) developed an integrated numerical model for the complete blow molding process, and simulated the blow molding of a gas tank. The viscoelastic deformations during parison formation and inflation were modeled by a K-BKZ constitutive equation, and the thermal dependence was accounted for by the Williams–Landel–Ferry (WLF) equation. Temperature variations during parison formation that affect the inflation were taken into account. They found good agreement with commercial size blow molding machine products.

Schmidt et al. (102) carried out a detailed experimental study of PET blow molding with a well-instrumented machine and compared the results with theoretical predictions using FEM and an Oldroyd B constitutive equation. They measured and calculated internal gas pressure, coupled it with the thermomechanical inflation and performed experiments and computations with free parison inflation.

Parison cooling is an integral part of the process that has been treated by a number of researchers (103–105). The principles are based on contact solidification without deformation, as discussed in Chapter 5. A special complication is the frictional heat generation in injection blow molding between the rod and the parison.

REFERENCES

1. J. F. Agassant, P. Coates, M. Denn, D. Edie, C. G. Gogos, K. S. Hyun, M. Kamal, H. Meijer, W. Michaeli, D. H. Sebastian, Z. Tadmor, J. Vlachopoulos, J. L. White, and M. Xanthos, (Organizing Committee), ''Touchstones of Modern Polymer Processing,'' Workshop Held at the Polymer Processing Institute at New Jersey Institute of Technology, Newark NJ, May 10–12, 2002. The quote is due to Han Meijer.
2. H. F. Mark, in *Rheology*, Vol. 4, F. R. Eirich, Ed., Academic Press, New York, 1969, Chapter 7.
3. J. R. Dees and J. E. Spruiell, ''Structure Development During Melt Spinning of Linear Polyethylene Fiber,'' *J. Appl. Polym. Sci.* **18**, 1053 (1974).
4. G. Capaccio and I. M. Ward, ''Ultra-high Modulus Linear Polyethylene through Controlled Modulus Weight and Drawing,'' *Polym. Eng. Sci.*, **15**, 219–224 (1975).
5. S. Kase and T. Matsuo, ''Studies on Melt Spinning, I. Fundamental Equations on the Dynamics of Melt Spinning,'' *J. Polym. Sci.*, Part A, **3**, 2541 (1965).
6. S. Kase and T. Matsuo, ''Studies on Melt Spinning, Part II. Steady State and Transient Solutions of Fundamental Equations Compared with Experimental Results, Fundamental Equations on the Dynamics of Melt Spinning,'' *J. Appl. Poly. Sci.*, **11**, 251–287 (1967).
7. M. A. Matovich and J. R. A. Pearson, ''Spinning a Molten Threadline,'' *Ind. Eng. Fundam.*, **8**, 512 (1969).
8. M. M. Denn, C. J. S. Petrie, and P. Avenas, ''Mechanics of Steady Spinning of Viscoelastic Liquids,'' *AIChE J.*, **21**, 791(1975).
9. R. J. Fisher and M. M. Denn, ''A Theory of Isothermal Melt Spinning and Draw Resonance,'' *AIChE J.*, **22**, 236–246 (1976).
10. T. C. Papanastasiou, C. W. Macosko, L. E. Scriven, and Z. Chen, ''Fiber Spinning of Viscoelastic Liquid,'' *AIChE J.*, **33**, 834–842 (1987).
11. P. W. Bell and D. D. Edie, ''Calculated Internal Stress Distribution in Melt-spun Fibers,'' *J. Appl. Polym. Sci.*, **33**, 1073–1088 (1987).
12. P. W. Bell and D. D. Edie, ''Measured Orientation and Internal Stress Distribution in Melt-spun Fibers,'' *J. Appl. Polym. Sci.*, **33**, 1089–1102 (1987).

13. J. A. Kulkarni and A. N. Beris, ''Lattice-based Simulation of Chain Conformation in Semi-crystalline Polymers with Application to Flow Induced Crystallization,'' *J. Non-Newt. Fluid Mech.*, **82**, 331–336 (1999).
14. A. K. Doufas, A. J. McHugh, and C. Miller, ''Simulation of Melt Spinning Including Flow-induced Crystallization. Part I. Model Development and Predictions,'' *J. Non-Newt. Fluid Mech.*, **92**, 27–66 (2000).
15. Y. L. Joo, M. D. Smith, R. C. Armstrong, R. A. Brown, and R. A. Ross, ''Two-dimensional Numerical Analysis of Non-isothermal Melt Spinning with and without Phase Transition,'' *J. Non-Newt. Fluid Mech*., **102**, 37–70 (2002).
16. R. Guennete and M. Fortin, ''A New Mixed Finite Element Method for Computing Viscoelastic Flows,'' *J. Non-Newt. Fluid Mech*., **77**, 153–190 (1998).
17. H. Giesekus, ''A Simple Constitutive Equation for Polymer Fluids Based on the Concept of Deformation-dependent Tensorial Mobility,'' *J. Non-Newt. Fluid Mech*., **11**, 60–109 (1982).
18. K. Nakamura, K. Katayama, and T. Amano, ''Some Aspects of Non-isothermal Crystallization of Polymers. Part II. Consideration of Isokinetic Conditions,'' *J. Appl. Polym. Sci*., **17**, 1031–1041 (1982).
19. A. Ziabicki, *Fundamentals of Fiber Formation*, Wiley, New York, 1976.
20. M. C. Levine, N. Waheed, and G. C. Rutledge, ''Molecular Dynamics Simulation of Orientation and Crystallization of Polyethylene during Uniaxial Extension,'' *Polymer*, **44**, 1771–1779 (2003).
21. Y. Ide and J. L. White, ''The Spinnability of Polymer Filaments,'' *J. Appl. Polym. Sci.*, **20**, 2511–2531 (1976).
22. C. J. S Petrie and M. M. Denn, ''Instabilities in Polymer Processing,'' *AIChE J*., **22**, 209 (1976).
23. Y. Ide and J. L. White, ''Investigation of Failure during Elongational Flow of Polymer Melts,'' *J. Non Newt. Fluid Mech.*, **2**, 281–298 (1977).
24. J. L. White and Y. Ide, ''Instabilities and Failure in Elongational Flow of Melts in Isothermal Spinning of Fibers,'' *J. Appl. Polym. Sci.*, **22**, 3057–3074 (1978).
25. S. Lee, B. M. Kim, and J. C. Hyun, ''Dichotomous behavior of Polymer Melts in Isothermal Mel Spinning,'' *Korean J. Chem. Eng.*, **12**, 345–351 (1995).
26. S. Kase, ''Studies in Melt Spinning, IV. On the Stability of Melt Spinning,'' J. *Appl. Polym. Sci*., **18**, 3279 (1974).
27. G. F Cruz-Saenz, G. J. Donnelly, and C. B. Weinberger, ''Onset of Draw Resonance during Isothermal Melt Spinning,'' *AIChE J.*, **22**, 441 (1976).
28. H. W. Jung and J. C. Hyun, ''Fiber Spinning and Film Blowing Instabilities,'' in *Polymer Processing Instabilities – Control and Understanding*, S. G. Hatzikiriakos and K. B. Migler, Eds., Marcel Dekker, New York, 2004, Chapter 11.
29. J. R. A. Pearson and Y. T. Shaw, ''Stability Analysis of the Fiber Spinning Process,'' *Trans. Soc. Rheol.*, **16**, 519–533 (1972).
30. Y. T. Shaw and J. R. A. Pearson, ''On the Stability of Non-isothermal Fiber Spinning – General Case,'' *Ind. Eng. Chem. Fundam.*, **11**, 150–153 (1972).
31. J. R. A. Pearson and Y. T. Shaw, ''On the Stability of Isothermal and Non-isothermal Fiber Spinning of Power Law Fluids, '' *Ind. Eng. Chem. Fundam.*, **13**, 134–138 (1974).
32. J. R. A. Pearson, Y. T. Shaw, and R. D. Mhaskar, ''On the Stability of Fiber Spinning of Freezing Fluids, '' *Ind. Eng. Chem. Fundam.*, **15**, 31–37 (1976).
33. R. J. Fisher and M. M. Denn, ''Finite-amplitude Stability and Draw Resonance in Isothermal Spinning,'' *Chem. Eng. Sci*., **30**, 1129–1134 (1975).
34. R. J. Fisher and M. M. Denn, ''Mechanics of Nonisothermal Polymer Melt Spinning,'' *AIChE J*., **23**, 23–28 (1977).

35. J. C. Chang and M. M. Denn, ''Sensitivity of the Stability of Isothermal Melt Spinning to Rheological Constitutive Assumptions,'' in *Rheology: Applications*, Vol. 3., G. Astarita, G. Marrucci, and L. Nicolais, Eds., Plenum Publishing, New York 1980, pp.9–13.
36. J. C. Chang, M. M. Denn, and F. T. Geyling, ''Effect of Inertia, Surface Tension and Gravity on the Stability of Isothermal Drawing of Newtonian Fluids,'' *Ind. Eng. Chem. Fundam.*, **20**, 147–149 (1981).
37. C. D. Han, *Rheology in Polymer Processing*, Academic Press, New York, 1976, Section 12.3.1.
38. I. J. Chen, G. E. Hagler, L. E. Abbott, D. C. Bogue, and J. L. White, ''Interpretation of Tensile and Melt Spinning Experiments in LDPE and HDPE,'' *Trans. Soc. Rheol.*, **16**, 473 (1972).
39. J. L White and Y. Ide, ''Instabilities and Failure in Elongational Flow and Melt Spinning of Fibers,'' *J. Appl. Polym. Sci*. **22**, 3057–3074 (1978).
40. B. M. Kim, J. C. Hyun, J. S. Oh, and S. J. Lee, ''Kinematic Waves in the Isothermal Melt Spinning of Newtonian Fluids,'' *AIChE J*., **42**, 3134–3169 (1996).
41. H. W. Jung, H.-S. Song, and J. C. Hyun, ''Draw Resonance and Kinematics Waves in Viscoelastic Isothermal Spinning,'' *AIChE J*., **46**, 2106–2111 (2000).
42. J. R. A. Pearson and C. J. S Petrie, ''The Flow of a Tubular Film. Part 1. Formal Mathematical Presentation,'' *J. Fluid Mech.*, **40**, 1–19 (1970).
43. J. R. A. Pearson and C. J. S Petrie, ''The Flow of a Tubular Film. Part 2. Interpretation of the Model and Discussion of Solutions,'' *J. Fluid Mech.*, **42**, 609–625 (1970).
44. J. R. A. Pearson and C. J. S. Petrie, *Plast. Polym.*, **38**, 85 (April 1970).
45. C. J. S. Petrie, ''A Comparison of Theoretical Predications with Published Experimental Measurements on the Blown Film Process,'' *AIChE J.*, **21**, 275–282 (1975).
46. W. Ast, ''Der Abkälvorgang bein Herstellen von Blasfolien aus Polyäthylen Niedriger Dichte,'' *Kunststoffe*, **63**, 427 (1973).
47. C. J. S. Petrie, in *Computational Analysis of Polymer processing*, J. R. A Pearson and S. M. Richardson, Eds., Applied Science Publishers, New York, 1983, Chapter 7.
48. J. R. A. Pearson, *Mechanics of Polymer Processing*, Applied Science Publishers, New York, 1985.
49. C. D. Han and J. Y. Park, ''Studies on Blown Film Extrusion, I. Experimental Determination of Elongational Viscosity,'' *J. Appl. Polym. Sci*., **19**, 3257 (1975).
50. C. D. Han and J. Y. Park, ''Studies on Blown Film Extrusion, II. Analysis of the Deformation and Heat Transfer Process,'' *J. Appl. Polym. Sci*., **19**, 3277 (1975).
51. C. D. Han and J. Y. Park, ''Studies on Blown Film Extrusion, III. Bubble Instability. Analysis of the Deformation and Heat Transfer Process,'' *J. Appl. Polym. Sci.*, **19**, 3291 (1975).
52. R. K. Gupta, Ph.D. Thesis, Department of Chemical Engineering, University of Delaware, Newark, NJ 1980.
53. T. Kanai and J. L. White, ''Kinematics, Dynamics and Stability of the Tubular Film Extrusion of Various Polyethylenes,'' *Polym. Eng. Sci*., **24**, 1185–1201 (1984).
54. T. Kanai and J. L. White, ''Dynamics, Heat Transfer, and Structure Development in Tubular Film Extrusion of Polymer Melts: A Mathematical Model and Prediction,'' *J. Polym. Eng*., **5**, 135 (1985).
55. V. Sidiropoulos and J. Vlachopoulos, ''An Investigation of Venturi and Coanda Effects in Blown Film Cooling,'' *Int. Polym. Process.*, **15**, 40 (2000).
56. V. Sidiropoulos and J. Vlachopoulos, ''The Effect of Dual-orifice Air-ring Design on Blown Film Cooling,'' *Polym. Eng. Sci*., **40**, 1611–1618 (2000).
57. V. Sidiropoulos and J. Vlachopoulos, ''Numerical Study of Internal Bubble Cooling in Film Blowing,'' *Int. Polym. Process.*, **16**, 48–53, (2001).

58. V. Sidiropoulos and J. Vlachopoulos, ''Temperature Gradients in Blown Film Bubbles,'' *Adv. Polym. Technol.*, **24**, 83–90 (2005).

59. G. A. Campbell, N. T. Obot, and B. Cao ''Aerodynamics in the Blown Film Process,'' *Polym. Eng. Sci*., **32**, 751 (1992).

60. X.-L. Luo and R. I. Tanner, ''A Computer Study of Film Blowing,'' *Polym. Eng. Sci.*, **25,** 620–629 (1985).

61. A. I. Leonov, ''Nonequilibrium Thermodynamics and rheology of viscoelastic polymer media,'' *Rheol. Acta*, **15**, 85–98 (1976).

62. J. J. Cain and M. M. Denn, ''Multiplicity and Instabilities in Film Blowing,'' *Polym. Eng. Sci*., **28**, 1527–1541 (1988).

63. D. Acierno, F. P. La Mantia, G. Marrucci, and G. Titomanlio, ''A Non-linear Viscoelastic Model with Structure-dependent Relaxation Times: I. Basic Formulation, '' *J. Non-Newt. Fluid Mech.*, **1**, 125–146 (1976).

64. C. D. Han, *Rheology in Polymer Processing*, Academic Press, New York, 1976, fig. 9.14.

65. J. C. Hyun, H. Kim, J. C. Lee, H. S. Song, and H. W. Jung, ''Transient Solutions of the Dynamics in Film Blowing Processes,'' *J. Non-Newt. Fluid Mech*., **121**, 157–162 (2004).

66. G. N. Beall and J. L. Throne, *Hollow Plastics Parts: Manufacturing and Design*, Hanser, New York, 2004.

67. D. V. Rosato, A. V. Rosato, and D. P. DiMatia, *Blow Molding Handbook*, Second Edition, Hanser, Munich, 2003.

68. M. L. Druin, ''PET Properties and Performance Requirements,'' paper presented at the Polyester Packaging - The Critical Path Ahead Conference, sponsored by Packaging Strategies, Inc., Newark, NJ, May 28–30 (1997).

69. N. Sheptak and C. E. Beyer, ''Study of Parison Formation, including the Effects of Swell and Drawdown,'' *Soc. Plastics Eng. J*., **32**, 190–196 (1965).

70. M. R. Kamal, V. Tan, and D. Kalyon, ''Measurement and Calculation of Parison Dimensions and Bottle Thickness Distribution during Blow Molding,'' *Polym. Eng. Sci*., **21**, 331–338 (1981).

71. M. R. Kamal and D. M. Kalyon, ''An Experimental Investigation of Capillary Extrudate Swell in Relation to Parison Swell Behavior in Blow Molding,'' *Polym. Eng. Sci*., **26**, 508–516 (1986).

72. A. Gracia-Rejon, R. W. DiRaddo, and M. E. Ryan, ''Effect of Die Geometry and Flow Characteristics on Viscoelastic Annular Die Swell,'' *J. Non-Newt. Fluid Mech*., **60**,107–128 (1995).

73. N. Orbey and J. M. Dealy, ''Isothermal Swell of Extrudate from Annular Dies; Effects of Die Geometry, Flow Rate, and Resin Characteristics,'' *Polym. Eng. Sci*., **24,** 511–518 (1984).

74. J. M. Dealy and N. Orbey, ''A Model for Parison Behavior in the Extrusion Blow Molding Process,'' *AIChE J*., **31**, 807–811 (1985).

75. A. H. Wagner and D. Kalyon, ''Parison Formation and Inflation Behavior of Polyamide-6 during Extrusion Blow Molding,'' *AIChE J*., **36**, 1897–1906 (1996).

76. D. Laroche, K. K. Kabanemi, L. Pecora, and R.W. DiRaddo, ''Integrated Numerical Modeling of the Blow Molding Process,'' *Polym. Eng. Sci*., **39**, 1223–1233 (1999).

77. S. Tanue, T. Kajiwara, K. Funatsu, K. Terada, and M. Yamabe, ''Numerical Simulation of Blow Molding – Prediction of Parison Diameter and Thickness Distribution in the Parison Formation Process,'' *Polym. Eng. Sci*., **36**, 2008–2017 (1996).

78. Y. Otsuki, T. Kajiwara, and K. Funatsu, ''Numerical Simulations of Annular Extrudate Swell Using Various Types of Viscoelastic Models,'' *Polym. Eng. Sci.*, **39**, 1969–1981 (1999).

79. B. Bernstein, E. A. Kearsley, and L. J. Zappas, ''A Study of Stress Relaxation with Finite Strain'', *Trans. Soc. Rheol*. **7**, 391–410 (1963).

80. M. H. Wagner, T. Raible, and J. Meissner, ''Tensile Overshoot in Uniaxial Extension of LDPE Melt,'' *Rheol. Acta*, **18**, 427–428 (1979).
81. J. T. Oden and T. Sato, ''Finite Strains and Displacements of Elastic Membranes by the Finite Element Method,'' *Int. J. Solids and Struct.*, **3**, 471–488 (1967).
82. J. M. A. Cesar de Sa, ''Numerical Modeling of Glass Forming Processes,'' *Eng. Comput.*, **3**, 266-275 (1986).
83. C. D. Denson, ''Implications of Extentioal Flow in Polymer Fabrication Processes,'' *Polym. Eng. Sci*., **13**, 125 (1973).
84. C. J. S. Petrie and K. Ito, ''Prediction of Wall Thickness of Blow Molded Containers,'' *Plast. Rubber Process*., **5**, 68-72 (1980).
85. H. G. deLorenzi and H. F. Nied, ''Finite Element Simulation of Thermoforming and Blow Molding,'' *SPE ANTEC Tech. Papers*, **33**, 418–420 (1987).
86. H. G. deLorenzi and H. F Nied, ''Blow Molding and Thermoforming of Plastics: Finite Element Modeling,'' *Compu. Struct*. **26**, 197–206 (1987).
87. H. G. deLorenzi, H. Nied, and C. A. Taylor, ''Simulation and Analysis of Blow Molding Using the Finite Element Method,'' *SPE ANTEC Tech. Papers*, **34**, 797–799 (1988).
88. H. F. Nied, C. A. Taylor, and H. G. deLorenzi, ''Three-dimensional Finite Element Simulation of Thermoforming,'' *Polym. Eng. Sci*., **30**, 1314–1322 (1990).
89. H. G. deLorenzi and H. F Nied in *Progress in Polymer Processing*, A. I. Isayev, Ed., Hanser Verlag, Munich, 1991.
90. J. M. Charrier, S. Shrivastava, and R. Wu, ''Free and Constrained Inflation of Elastic Membranes in Relation to Thermoforming - non-axisymmetric Problems,'' *J. Strain Anal.*, **24**, 55–74 (1989).
91. G. Marckmann, E. Verron, and B. Peseux, ''Finite Element Analysis of Blow Molding and Thermoforming Using a Dynamic Explicit Procedure,'' *Polym. Eng. Sci*., **41**, 426–439 (2001).
92. E. Verron, G. Marckmann, and B. Peseux, ''Dynamic Inflation of Non-Linear Elastic and Viscoelastic Rubber-like Membranes,'' *Int. J. Num. Meth. Eng*. **50**, 1233–1251 (2001).
93. D. Laroche, K. K. Kabanemi, L. Pecora, and R. W. Diraddo, ''Integrated Numerical Modeling of the Blow Molding Process,'' *Polym. Eng. Sci*., **39**, 1223–1233 (1999).
94. M. H. Vantal, B. Monasse, and M. Bellet, *Numiform*, **95**, 1089 (1995).
95. A. Rodriguez-Villa, J. F. Agassant, and M. Bellet, ''Finite Element Simulation of the Extrusion Blow-Molding Process,'' *Numiform*, **95**, 1053 (1995).
96. S. Wang **,** A. Makinouchi, and T. Nakagawa, ''Three-dimensional Viscoplastic FEM Simulation of a Stretch Blow Molding Process,'' *Adv. Polym. Technol*., **17**, 189–202 (1998).
97. K. Kouba and J. Valchopoulos, ''Modeling of Thermoforming and Blow Molding,'' *Theoretical and Applied Rheology*, *Proc. XIth Cong. Rheology*, Brussels, Belgium, August 17–21, 1992.
98. B. Debbaut, B. Hocq, and J. M. Marchal, ''Numerical Simulation of the Blow Molding Process,'' *SPE ANTEC Tech. Papers*, **39**, 1870–1872 **(**1993).
99. B. Debbaut, B. Hocq, J. M. Marchal, Y. Jiang, and V. Legat, ''Blow Molding: a 3D Approach,'' *Proc. III World Congr. on Computational Mechanics*, IACM, Chiba, Japan, 1994, pp. 1580–1581.
100. S. Shrivastava and J. Tang, ''Large Deformation Finite Element Analysis of Non-linear Viscoelastic Membranes With Reference to Thermoforming,'' *J. Strain Anal*. **28**, 31 (1993).
101. D. Laroche, K. K. Kabanemi, L. Pecora, and R. W. DiRaddo, ''Integrated Numerical Modeling of the Blow Molding Process,'' *Polym. Eng. Sci*., **39**, 1223–1233 (1999).
102. F. M. Schmidt, J. F. Aggasant, and M. Bellet, ''Experimental Study and Numerical Simulation of the Injection Stretch/Blow Molding Process,'' *Polym. Eng, Sci.*, **38**, 1399–1407 (1998).
103. M. F. Edwards, P. K Suvanaphen, and W. L. Wilkinson, ''Heat Transfer in Blow Molding Operations,'' *Polym. Eng. Sci.* **19**, 910 (1979).

104. M. F. Edwards, S. Georghiades, and P. K. Suvanaphen, *Plast. Rubber. Compos. Process. Appl.*, **1**, 161 (1981).

105. M. R. Kamal and D. Kalyon, "Heat Transfer and Microstructure in Extrusion Blowmolding," *Polym. Eng. Sci.*, **23**, 503–509 (1983).

PROBLEMS

14.1 ***Isothermal Fiber Spinning of a Newtonian Melt***[4] In carrying out this analysis, neglect (i) any heat transfer to the surrounding air, that is, assume that the fiber drawing is completed over a very short distance downstream from the spinneret and then quenched in a liquid medium; (ii) the air-drag forces as well as the surface-tension forces that arise from the rapid generation of new surface during drawing. The relevant stresses, velocity, surface vectors **t** and **n**, and coordinates are shown in the accompanying figure for a representative section of the fiber being drawn in air.

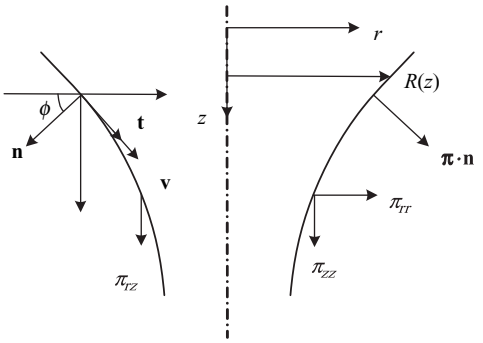

where $\pi_{il} = P + \tau_{li}$ and $\pi_{ij} = \tau_{ij}$ $(i \neq j)$. Assume that $v_z = v_z\,(r, z)$, $v_r = v_r\,(r, z)$, $P = P\,(r, z)$, and Newtonian constitutive equation $\pi_{zz} = P - 2\mu(\partial v_z/\partial z)$

(a) Derive the following expression for the z-component velocity and resulting fiber radius

$$R(z) = R_0 \exp\left[-\frac{1}{2} z \frac{\ln D_R}{L}\right]$$

where $D_R = V_L/V_0$, V_0 and R_0 are values at the spinneret exit, and L is the length of the drawdown region

(b) If nylon 6–6 is extruded at a volumetric flow rate of $0.1\,\text{cm}^3/\text{s}$, at 285°C and drawn under isothermal conditions in a chamber of $L = 400\,\text{cm}$, $D_R = 100$, with a take up speed of 1000 m/min, and if the extrudate swell diameter is three times that of the spinneret diameter, calculate: (1) the maximum stretching rate of the drawn nylon 6–6 melt, and (2) the maximum tensile stress in the melt and the force needed to draw the fiber

4. D. G. Baird and D. I. Collias, *Polymer Processing*, Wiley, New York, 1998, Chapter 9; also, S. Middleman, *Fundamentals of Polymer Processing*, McGraw-Hill, New York, 1997, Chapter 9.

14.2 ***Relative Importance of the Various Terms in the Analysis of the Isothermal Fiber Spinning of a Newtonian Melt*** Use the data and result of Problem 14.1(b) to evaluate the importance in the isothermal fiber spinning of a Newtonian melt analysis (nylon 6-6 at 285°C) of the inertial terms and gravity relative to the viscous stress terms. Using Eq. E14.1-2 for F_D, evaluate the importance of the air-drag force term.

14.3 ***Isothermal Fiber Spinning of a Power Law Melt*** Derive the following expression for the axial velocity $v_z(z)$ resulting from the steady isothermal fiber spinning of a Power Law melt

$$v_z(z) = v_0\left[1 + \left(D_R^{(n-1)/n} - 1\right)\frac{z}{L}\right]^{n/(n-1)}$$

Use the assumption made in Problem 14.1

14.4 ***Transport Equations for Nonisothermal Fiber Stretching*** Starting from the momentum and thermal energy balances, derive Eqs. E14.1-1 and E14.1-3, which are used for the description of the nonisothermal stretching of molten polymer fibers. (a) Discuss in detail the assumptions made, and specifically discuss the nature of F_D and its inclusion in the momentum balance (e.g., "Where did it come from?"); the relative magnitude of gravity (use real $\bar{\eta}$ and $\dot{\varepsilon}$ data); the form of the entire Eq. 14.1-3 and the absence of radial temperature gradients. (b) What additional complexities to the solution of the problem would the inclusion of dT/dr bring?

14.5 ***Estimation of $T(r = 0, t)$* in Melt-Spun Fibers** (a) From $T(x_1, \alpha t)$ values of the accompanying figure (x_1) is the characteristic length equivalent to the radius of the cylinder) calculate the centerline temperature of a HDPE melt strand exiting the spinneret at 240°C at a take-up speed of 50 m/min, a mass flow rate of 1.93 g/min, at distances 50 cm and 10 cm below the spinneret plate. Assume that no change in phase occurs and that the heat-transfer coefficient is $10^{-3}\,\mathrm{cal/cm^2 \cdot s \cdot K}$, $k = 8 \times 10^{-4}\,\mathrm{cal/cm \cdot s \cdot K}$, $\rho = 0.75\,\mathrm{g/cm^3}$, $C_p = 0.5\,\mathrm{cal/g}$, and the cooling-medium temperature is 25°C. (b) What can you conclude about the magnitude of dT/dr relative to dT/dz?

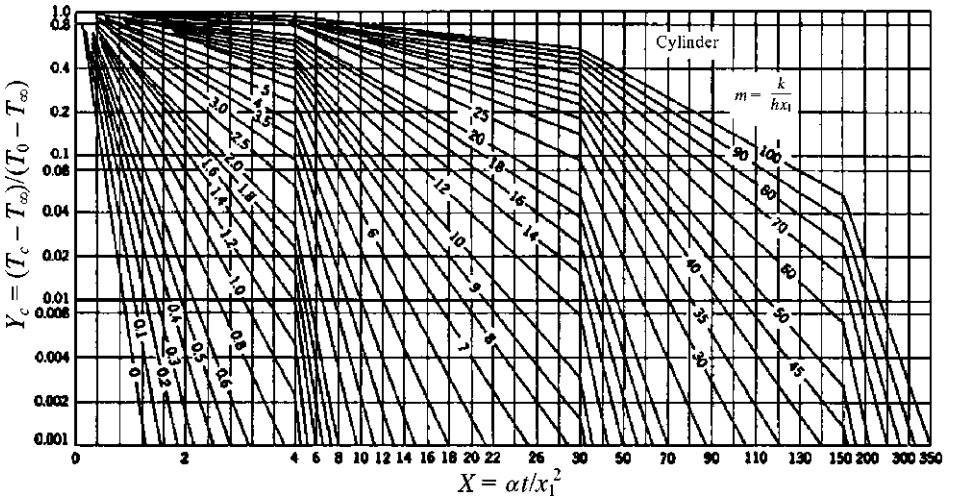

14.6 ***Isothermal Film Casting of a Newtonian Melt***[5] The film casting process is shown schematically on the accompanying figure.

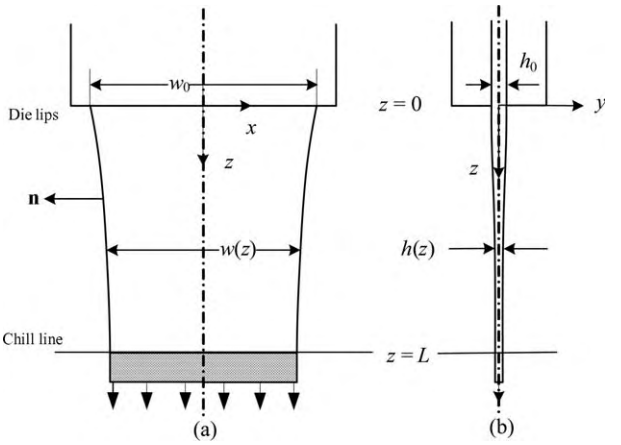

For very thin films $|\nabla h \ll 1|$, both h and w decrease with increasing z. The analysis of this case for a Newtonian melt being film cast nonisothermally has been treated by Pearson [J. R. A. Pearson, *Mechanics of Polymer Processing*, Elsevier, New York, 1985]. (a) For thicker films the deformation of the melt can be considered as one where only $h = h(z)$ and $w = w_0$. Use the continuity and z-momentum equations, neglecting inertial terms, gravity, and air-drag forces, to obtain the following expressions for $h(z)$ and $v_z(z)$:

$$h(z) = h_0 \exp\left(\frac{-z\rho F}{\bar{\eta}_{pl}\dot{m}}\right) = h_0 D_R^{-z/L}$$

$$v_z(z) = v_{z0} \exp\left(\frac{-z\rho |F|}{\bar{\eta}_{pl}\dot{m}}\right) = v_{z0} D_R^{-z/L}$$

where

$$D_R = \exp\left(-\frac{\rho F L}{\bar{\eta}_{pl}\dot{m}}\right)$$

F is the force necessary to draw the film, ρ is the melt density, and $\bar{\eta}_{pl} = 4\mu$, thus, $\pi_{zz} = -4\mu(dv_z/dz)$.

(b) Prove that the following relationship holds for isothermal and Newtonian fiber spinning and film casting:

$$\frac{[\ln D_R]_{\text{spin.}}}{[\ln D_R]_{\text{cast.}}} = \frac{4}{3}$$

5. D. G. Baird and D. I. Collias, *Polymer Processing*, Wiley, New York, 1998, Chapter 9.

14.7 ***Free Sheet Blowing*** Free bubble blowing of heat-softened polymeric sheets is a good test for thermoformability of polymers.[6] The bubble behaves as a membrane with rotational symmetry, as shown in the accompanying figure. The shape of the membrane is specified by a meridian curve $r(z)$ and the thickens distribution $\delta(z)$. The two principal radii of curvature of the surface R_L and R_C, in the meridian (longitudinal) and circumferential (hoop) directions, respectively, are related to $r(z)$ as follows:

$$R_C = r\sqrt{1 + (dr/dz)^2} \qquad R_L = \frac{[1 + (dr/dz)^2]^{3/2}}{d^2r/dz^2}$$

By symmetry, the two principal directions of stress (and strain) are in the meridian direction, π_{11}, and the circumferential direction π_{33}. The third principal stress is zero. Show that if body and acceleration forces are neglected, the following equilibrium equations are obtained for thin membranes:

$$\Delta P = -\delta\left(\frac{\pi_{11}}{R_L} + \frac{\pi_{33}}{R_C}\right)$$

$$-\frac{d}{dz}(r\delta\pi_{11}\cos\theta) = r\left(\frac{dr}{dz}\Delta P\right)$$

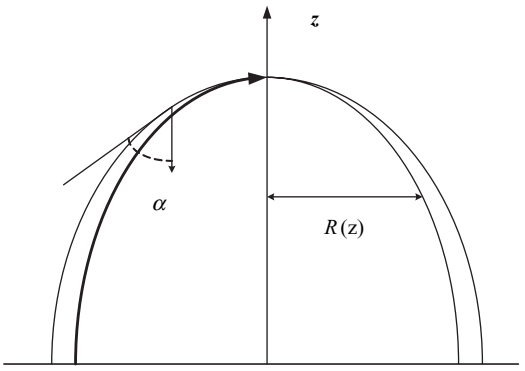

14.8 ***Wall Thickness Distribution in a Conical Mold*** Consider a thermoforming process of heat-softened polymeric sheet of thickness h_0 into a cold conical mold, as shown in the accompanying figure. Assuming incompressible polymer, elastic deformation, uniform spherical bubble thickness at the time of contacting the conical mold, frictionless contact, and immediate freezing of the plastic upon contact, show the thickness distribution is given by:

$$\frac{h}{h_0} = \frac{1 + \cos\beta}{2}\left(1 - \frac{z_k}{H}\sin\beta\right)^{\sec\beta - 1}$$

6. L. R. Schmidt and J. F. Carley, "Biaxial Stretching of Heat Softened Plastic Sheets: Experiments and Results," *Polym. Eng. Sci.*, **15**, 51–62 (1975).

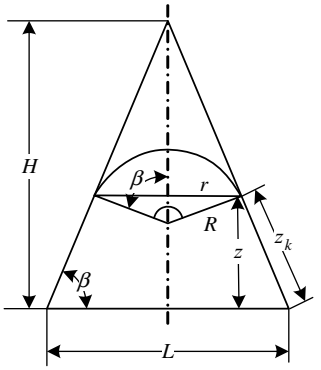

14.9 ***Wall Thickness–Thermoforming a Cup*** Consider a cup 6 cm in diameter throughout its height and 10 cm high, which has to be made out of a 1.5-mm-thick molten high impact polystyrene (HIPS) sheet. Derive an expression for the thickness distribution assuming that the free bubble is of spherical shape until its top reaches the mold bottom, once the bubble touches the mold, no further deformation occurs, and the thickness of the free bubble at any stage of its deformation is spatially uniform. Once the melt touches the bottom of the mold, the deformation that fills the corners can be represented by spherical sections of successively smaller radii and centers that move diametrically to the corners.

14.10 ***Blown Film Deformation during Folding by the "Tent" and the Nip Rolls***[7] In the film blowing process the solidified round film bubble comes into contact with a series of guides (slats or rollers) that form the "tent," and gradually collapses into a folded configuration between the nip rolls. Folding the bubble and feeding it into the nip rolls impose a deformation on the film, which is a function of the angle θ in the plane of the cross section of the bubble. The deformation results from the fact that each "fiber" of the film, that is, at each θ, travels a distance $L(\theta)$ that is different from the last round cross section to the nip rolls. Derive an expression for this deformation. What effect does it have on the wrapping step following the slitting?

7. William Arruda, private communication.